The Pennsylvania State University
The Graduate School

# COMPUTATION OF TWO-PHASE DRAG REDUCTION BY GAS INJECTION

A Thesis in
Mechanical Engineering
by
Daniel Maciejewski



Submitted in Partial Fulfillment
of the Requirements
for the Degree of

Master of Science

August 2012

The thesis of Daniel Maciejewski was reviewed and approved* by the following:

Eric G. Paterson
Professor of Mechanical Engineering
Senior Scientist, Applied Research Laboratory
Thesis Co-Advisor

Scott T. Miller
Research Associate, Applied Research Laboratory
Thesis Co-Advisor

Jonathan S. Pitt
Research Associate, Applied Research Laboratory

Gita Talmage
Professor of Mechanical Engineering

Karen A. Thole
Professor of Mechanical Engineering
Head of Mechanical and Nuclear Engineering

*Signatures are on file in the Graduate School.

# Abstract

The skin friction drag on ships and other solid bodies moving through water can be reduced by introducing air through the solid surface into the attached turbulent boundary layer. This phenomenon is known as microbubble drag reduction (MBDR), or simply bubble drag reduction (BDR). Air is typically introduced through micropores in sintered plates or through thin slots. Continuing experimental efforts since the 1970s have revealed several physical mechanisms acting in the two-phase mixture to cause a localized reduction in skin friction. Motivated to reduce total vehicle drag, researchers in this field have focused on finding the functional dependence of the drag reduction.

A homogeneous, two-phase, compressible computational flow solver is used to simulate these flows. The homogenized fluid's mixture properties are determined from local volume fractions of air and water. Air injection is modeled with a volumetric source term for mass balance rather than a boundary condition on velocity. Mixing of phases after injection is modeled through use of a turbulent dispersion term. Experiments conducted by Madavan, Deutsch and Merkle (1984) in the twelve-inch water tunnel at ARL/PSU are used for validation. Good agreement between experiment and model is found for the total drag reduction with air injection. The return to no-injection skin friction values downstream of the injection region is also predicted by the model. Agreement with experiment is found for both single phase simulations and multiphase simulations with gas injection. Validation was achieved by comparison of velocity profiles and wall-shear profiles between simulation and experiment.

# Table of Contents


**List of Figures** **vi**

**List of Tables** **vii**

**List of Symbols** **viii**

**Acknowledgments** **xi**

**Chapter 1 Introduction** **1**

**Chapter 2 Literature Review** **4**
- 2.1 Characteristics of a single phase turbulent boundary layer . . . 4
- 2.2 Experimental literature . . . 5
- 2.3 Analytic models . . . 12
- 2.4 Numerical models . . . 15
- 2.5 Summary . . . 20

**Chapter 3 Governing Equations and Multiphase Model** **21**
- 3.1 Governing equations . . . 21
- 3.2 Multiphase model . . . 22
  - 3.2.1 Equations of state . . . 23
    - 3.2.1.1 Phase 1: Isentropic gas . . . 23
    - 3.2.1.2 Phase 2: Compressible liquid . . . 23
  - 3.2.2 Volume fraction equation . . . 24
  - 3.2.3 Pressure equation . . . 24
  - 3.2.4 Spalart-Allmaras turbulence model . . . 24
  - 3.2.5 Turbulent dispersion . . . 24
  - 3.2.6 Gas injection model . . . 25
  - 3.2.7 New volume fraction and pressure equations . . . 26
- 3.3 Finite volume method . . . 26
- 3.4 Approach to simulations . . . 28

**Chapter 4 Computations** **29**
4.1 Single phase validation . . . 29
4.1.1 Computational domain . . . 29
4.1.2 Boundary conditions and material properties . . . 30
4.1.3 Computational mesh . . . 31
4.1.4 Single phase simulations . . . 32
4.1.5 Single phase velocity profiles . . . 32
4.1.6 Single phase skin friction . . . 35
4.2 Multiphase simulations . . . 36
4.2.1 Case setup and test matrix . . . 36
4.2.2 Gas concentration profiles . . . 38
4.2.3 Velocity profiles . . . 39
4.2.4 Wall shear profiles . . . 40
4.2.5 Dispersion coefficient study . . . 40
4.2.6 Gravitational effects . . . 41
4.2.7 Drag results . . . 42

**Chapter 5 Summary** **45**
5.1 Computational results . . . 46
5.2 Future work . . . 46

**Appendix A Analysis of Kolmogorov scales with microbubble injection** **47**

**Bibliography** **51**

# List of Figures


2.1 Incompressible TBL over a flat plate . . . 5
2.2 Gas volume fraction profiles . . . 7
2.3 Water tunnel experimental setup . . . 8
2.4 Drag ratio vs. airflow rate . . . 9
2.5 Drag ratio vs. $C_q$ . . . 9
2.6 Skin friction ratio and plate orientation . . . 11
2.7 Bubble forces . . . 15
2.8 Mixture viscosity ratios . . . 16
2.9 Imposed gas fraction profile . . . 17
2.10 Predicted velocity profiles . . . 18
2.11 Predicted Drag . . . 18

4.1 Determination of virtual origin . . . 30
4.2 Numerical grid with mesh regions . . . 31
4.3 Single phase velocity profiles . . . 33
4.4 Single phase velocity profiles in outer variables . . . 33
4.5 Single phase velocity profile in inner variables . . . 34
4.6 Single phase wall shear stress profile . . . 35
4.7 Single phase computed and empirical skin friction . . . 36
4.8 Gas fraction profiles $\alpha(y)$ . . . 38
4.9 Velocity profiles $u(y)$ . . . 39
4.10 Wall shear stress along test surface . . . 40
4.11 Drag ratio as a function of $C_{\text{disp}}$ . . . 41
4.12 Drag ratio vs. changing plate orientation . . . 42
4.13 Comparison of experimental and computed drag ratios . . . 43
4.14 Drag Ratio vs. $C_q$ . . . 44
4.15 Comparison of sublayer and wall function mesh drag ratios . . . 44

A.1 Change in microscales of turbulence . . . 49

# List of Tables

3.1 Numerical schemes used for interpolation and differentiation . . . . . . . . . . . . 27
3.2 Tolerances on linear equation solvers . . . . . . . . . . . . . . . . . . . . . . . . . . 28

4.1 Water properties specified for single phase simulations . . . . . . . . . . . . . . . . 31
4.2 Free stream speeds and corresponding Reynolds numbers . . . . . . . . . . . . . . 32
4.3 Air flow rates . . . . . . . . . . . . . . . . . . . . . . . . . . . . . . . . . . . . . . . 37
4.4 $C_q$ values for air injection cases . . . . . . . . . . . . . . . . . . . . . . . . . . . . 37
4.5 Air properties specified for multiphase simulations . . . . . . . . . . . . . . . . . . 37

# List of Symbols

**Abbreviations**

| | |
|---|---|
| EOS | equation of state |
| MBDR | microbubble drag reduction |
| TBL | turbulent boundary layer |

**English Letters**

| | |
|---|---|
| $A$ | area of gas injection |
| $b$ | injector width |
| $c$ | speed of sound |
| $D$ | drag, diffusion coefficient |
| $D_0$ | drag of unmodified flow |
| $\mathbf{D}$ | symmetric stretching tensor |
| $\mathbf{g}$ | gravity vector |
| $\mathbb{I}$ | identity tensor |
| $p$ | pressure |
| $q$ | turbulent velocity scale |
| $Q$ | volumetric gas injection rate |
| $Q_a$ | volumetric flux of air in boundary layer |
| $Q_w$ | volumetric flux of water in boundary layer |
| $\mathbf{T}$ | Cauchy stress tensor |
| $\mathbf{u}$ | velocity vector |
| $U_\infty$ | free-stream liquid velocity |
| $u$ | streamwise velocity component |

$v$ velocity component normal to wall, Kolmogorov velocity scale

$x$ streamwise coordinate

$y$ wall-normal coordinate, mass fraction

**Greek Letters**

$\alpha$ gas volume fraction

$\gamma$ ratio of specific heats

$\delta$ boundary layer thickness

$\delta^\star$ boundary layer displacement thickness

$\epsilon$ turbulent dissipation rate

$\eta$ Kolmogorov length scale

$\theta$ boundary layer momentum thickness

$\lambda$ bulk viscosity

$\Lambda$ length scale of energy-containing eddies

$\mu$ dynamic (shear) viscosity

$\nu$ kinematic viscosity

$\xi$ kinematic viscosity ratio

$\rho$ density

$\tau$ shear stress, Kolmogorov time scale

**Dimensionless Groups**

$C_D$ drag coefficient

$C_{D0}$ drag coefficient of unmodified flow

$C_{\mathrm{disp}}$ dispersion coefficient

$C_f$ skin-friction coefficient

$C_{f0}$ skin-friction coefficient of unmodified flow

$C_q$ gas injection blowing parameter

$C_v$ volume fraction of boundary layer occupied by gas

$Re$ Reynolds number

$Sc$ Schmidt number

**Subscripts**

$_0$ single phase liquid flow

$_t$ turbulent

$_w$ wall

**Superscripts**

$^+$ inner-variable scaled coordinate

# Acknowledgments

I would like to acknowledge my family for their support during my years of undergraduate and graduate education here at Penn State.

I appreciate the challenge posed by this problem, and the opportunity provided by Dr. Eric Paterson and Dr. Scott Miller to make this investigation. They have helped me grow as a researcher and a person, and have shared their personal insight and experience, which has not been limited to the technical issues presented by this study. Dr. Jon Pitt has also provided valuable insight and encouragement for this work.

Furthermore I would like to thank my fellow students, the faculty and staff of the Garfield Thomas Water Tunnel. The Applied Research Laboratory's Walker Graduate Assistantship allowed me the freedom to focus on studies and research, and the support is much appreciated.

Chapter 1

# Introduction

Launch of an underwater vehicle from a dry, gas-filled tube involves two-phase flow as soon as launch begins and the vehicle enters the water. In the vehicles motivating this study, a substantial volume enclosed by the outer casing is void space, filled with gas while the vehicle resides in the tube. As the gas pressure inside this void space is greater than the surrounding water pressure, gas is ventilated into the flow of water over the body by small holes in the vehicle. Forces from the fluid flow at the surface together with gravity determine the trajectory of the vehicle. As the body accelerates, a turbulent boundary layer (TBL) forms on the surface of the vehicle. Determination of frictional drag due to single phase turbulent boundary layers has been studied for nearly a century and is well understood. However, the gases introduced from the surface interact with the TBL to reduce the frictional resistance on the surface. Accurate prediction of surface forces in the presence of the ventilated gases is the objective of this research.

Development of an accurate Computational Fluid Dynamics (CFD) model of underwater launch is desirable as a design tool, as determination of vehicle travel underwater is important. Modern CFD methods and computers can give designers knowledge of the entire flow field and allow studies of possible design changes much more quickly and cheaply than experiments. This model must include the effect of ventilated gases on the flow field, and thus on the forces experienced by the body. The primary goal of the CFD tool, calculation of vehicle trajectory, determines the level of modeling accuracy needed for the gas ventilation taking place. Six degree-of-freedom calculation of the vehicle's rigid body motion only requires the net forces and moments acting on the body to be known; local variations in surface forces are not important. The implication for gas injection is that high fidelity modeling of the details of injection is not only unnecessary, but also that such details would be lost in the integration process.

A simplified model of gas injection is developed in this thesis which captures the change in forces due to gas injection, while realizing some computational efficiencies due to its simplicity. Simplifications are made to both the geometry and the mathematical model.

Geometric simplifications are made to the injection sites. The holes from which gas is ventilated are very small compared to the overall vehicle size. To accurately resolve this geometry would require mesh concentration at all injection sites, causing the total mesh size to increase substantially. This high-fidelity mesh would require increased computational resources for solution, along with detailed boundary condition information which is not known. Specifically, air velocity at each injection port would need to be specified. Pressure inside the vehicle at any time after launch can be estimated from its initial value and the total gas volume that has left the vehicle up to that time. Pressure in the environment outside the vehicle is known from the depth of the vehicle in water. The total area available for injection is known from the detailed geometry of the vehicle. Thus, the total air flow rate from the vehicle can be calculated based on the pressure difference and available injection area. Knowledge of air velocities at the individual ports cannot be known with this information alone. The whole region containing many injection holes can be modeled as having a uniform air flow rate, determined from the total pressure difference, void volume of the vehicle and available injection area. As such, our our simplified geometric model uses a single gas injection region rather than multiple discrete injection sites.

As will be seen in the literature review, there are several physical mechanisms by which the bubbles resulting from injection decrease the skin friction on the surface. The phenomenon of the drag reduction effect from air injection is known as microbubble drag reduction (MBDR). The dominant physical mechanism is the reduction of mixture density due to the high mixture gas fraction near injection. Other mechanisms, such as enhanced turbulence dissipation and modification of turbulence, further reduce drag but can be neglected in comparison to the effect of reduced mixture density. Furthermore, these secondary mechanisms require a more complex two-fluid model, while the homogeneous model used here successfully captures the density effect. The effect of turbulent dispersion is also accommodated in the present model, which acts to decrease the fraction of gas near the wall downstream of the injection region. Through incorporation of these two physical mechanisms good drag reduction results are obtained. The mathematical model used herein is simplified by only considering the density reduction and turbulent dispersion mechanisms.

Experimental studies of MBDR have used flat plate geometries with a single porous injection section. Use of a single region for gas injection in these studies is in keeping with the simplified-geometry approach to gas injection advocated above. While the body shape of an underwater vehicle is not a flat plate, an axisymmetric shape can be approximated as a flat plate if curvature can be neglected. Simulations of a flat plate turbulent boundary layer with gas injection from a single section are presented in Chapter 4. This allows validation against available experimental results and allows the use of two-dimensional simulations. Thus geometric complexities are avoided, which is desirable in the early development of the model.

The thesis takes the following form. Chapter 2 is a literature review of the experimental, analytical, and numerical efforts made on the problem of microbubble drag reduction. Several explanations for the drag reduction effect are presented from the literature. Chapter 3 presents the numerical model used in the study, and identifies two new equation terms which have been added to model microbubble drag reduction. Chapter 4 describes the single phase and multiphase simulations that have been performed and provides some analysis of the results. Finally, Chapter 5 provides major conclusions from this study and suggests future work for application and improvement of this model.

Chapter 2

# Literature Review

The skin-friction drag in a turbulent, wall-bounded flow of water can be reduced by introducing air or other gases from the wall into the flow. Depending on the bulk flow parameters of the liquid and the details of gas injection, including volumetric fluxes of gas and injector geometries, very different flow regimes can exist. Experimental investigations of microbubble drag reduction are surveyed, followed by analytic and numerical modeling efforts.

## 2.1 Characteristics of a single phase turbulent boundary layer

The literature on microbubble drag reduction in turbulent, wall-bounded flow describes how the presence of the microbubbles modifies a single phase turbulent boundary layer (TBL) at the same speed and on the same geometry (the baseline case or unmodified flow). Understanding this literature requires a working knowledge of turbulent flow, especially at a wall, i.e. the classical flat-plate turbulent boundary layer. Since turbulence is too complex to be described exactly, often major characteristics are pointed out. The five characteristics identified by White (1991, chap. 6) are quoted here:

1. *Fluctuations* in pressure and velocity (and also temperature when there is heat transfer). Velocity fluctuates in all three directions. Fluctuations are superimposed upon a mean value of each property.
2. *Eddies* or fluid packets of many sizes, which intermingle and fill the shear layer. Eddy size varies continuously from shear-layer thickness $\delta$ down to the Kolomogorov length scale.
3. *Random* variations in fluid properties which have a particular form (not white noise). Each property has a specific continuous energy spectrum which drops off to zero at high wave numbers (small eddy size).

4. *Self-sustaining* motion. Once triggered, turbulent flow can maintain itself by producing new eddies to replace those lost by viscous dissipation. This is especially so in wall-bounded flows. Turbulence production is not generally related to the original instability mechanisms such as Tollmien-Schlichting waves.

5. *Mixing* which is much stronger than that due to laminar (molecular) action. Turbulent eddies actively move about in three dimensions and cause rapid diffusion of mass, momentum, and energy. Ambient fluid from nonturbulent zones will be strongly entrained into a turbulent flow. Heat transfer and friction are greatly enhanced compared to laminar flow. Turbulent mixing is associated with a gradient in the time-mean flow.

An illustration of many of White's points is given by Figure 2.1. The beautiful complexity of this flow shows many turbulent eddies, the curled-up structures. As the turbulence 'reaches out' into the flow, we can see how the ambient fluid (black) is entrained into the TBL, leading to its fast growth. This image also suggests strong mixing, which is critical to this work. It is the strong mixing which brings the momentum of the free stream very close to the surface of the plate, leading to the high surface stresses and thus drag which are necessary to balance this high momentum. Finally, even the bubbles themselves, which act to reduce the surface stresses, are themselves eventually removed from the vicinity of the wall by this same mixing. Its complexity and importance to engineering applications makes turbulence a subject of intense research.

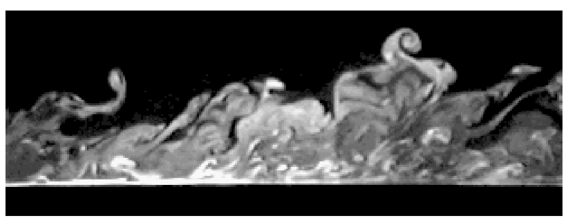

**Figure 2.1.** Laser-induced fluorescence image of an incompressible turbulent boundary layer over a flat plate, flow from left to right. (C. Delo)

## 2.2 Experimental literature

Before beginning the experimental review for this thesis, it is noted that an extensive review of all experimental efforts in microbubble drag reduction research up to the time of its publication was made by Charles Merkle and Steven Deutsch of Penn State (Merkle & Deutsch, 1992). It should also be noted that the motivation for microbubble drag reduction (MBDR) research is to gain an understanding of the relevant physics so that such understanding can be applied to reduce propulsion costs in water transport.

To quantify the effect of skin friction reduction, a local measure or an integrated measure can be employed. Let $\tau_w$ be the local, time-averaged skin friction at any point on the wall in the presence of microbubbles, and $\tau_{w0}$ be the local time-averaged skin friction at the same point in the corresponding flow without microbubbles. Then the skin friction ratio, a local measure, is

$$\text{Friction Ratio} = \frac{\tau_w}{\tau_{w0}}. \tag{2.1}$$

Similarly, let $D$ be the time-averaged drag measured over some finite area (usually a force balance in experiments) in the presence of microbubbles, and $D_0$ be the time-averaged drag on the same area in the corresponding flow without microbubbles. Thus, the drag ratio, an integrated measure is

$$\text{Drag Ratio} = \frac{D}{D_0}. \tag{2.2}$$

Generally, drag includes two components: friction drag and pressure drag. Since all measurements discussed here are on flat plates, the only component of drag is friction drag, and therefore no complications are introduced by nonuniform pressure distributions.

McCormick and Bhattacharya (1973) reported the first microbubble experiments. They towed an axisymmetric body wrapped with copper wire. A current was passed through the wire and hydrogen gas was produced from electrolysis in the water. Significant vehicle drag reduction was reported, which was shown to increase with gas generation rate and decrease with vehicle speed. This work showed that drag reduction from microbubbles was possible and motivated further work (Merkle & Deutsch, 1992).

Three experimental studies were reported in the Soviet Union after the work of McCormick and Bhattacharya (Migirenko and Evseev, 1974; Bogdevich and Evseev, 1976; Bogdevich and Malyuga, 1976; and Dubnischev et al, 1975). By injecting air through a porous material into a nominally zero-pressure-gradient TBL, local skin friction reductions up to 80% were measured. Soviet measurements revealed two important characteristics of the bubble concentration downstream of the injection section. First, the bubble (gas) concentration $\alpha$ approaches zero very near the wall, as can be seen in Figure 2.2. Second, the gas concentration peaks deep within the boundary layer, near $y/\delta = 0.1$ or 0.2, where $\delta$ is the boundary layer thickness (Merkle & Deutsch, 1992).

Also note the changing shape of the gas concentration profiles in the three frames of Figure 2.2. The concentration peak is sharpest in the left frame, with free stream velocity of the water $U_\infty = 10.9$ m/s, while it is flattest in the right frame, where $U_\infty = 4.36$ m/s. This suggests a changing balance between advection and the two forces acting to move the bubbles away from the wall: lift from the mean velocity gradient and buoyancy. In this experiment, the plate is on the bottom of the test section, so buoyancy is acting with lift to move the bubbles away from the wall. When advection is strongest (high free stream speeds) the bubbles remain closer to the wall at any fixed downstream location compared to when advection is weaker (lower speeds). Further, Merkle & Deutsch (1992) note that the Soviet data show a monotonic decrease in the mean velocity gradient very near the wall as gas injection rate is increased. This decreased velocity gradient near the wall correlates directly with a decrease in wall shear.

Merkle & Deutsch (1992) discuss the proper nondimensionalization for the volumetric air

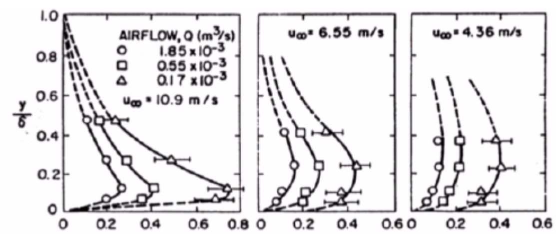


**Figure 2.2.** Gas volume fraction profiles. (Migirenko and Evseev, 1974)

injection rate $Q$. A straight-forward choice is the blowing parameter

$$C_q = \frac{Q}{AU_\infty}, \tag{2.3}$$

where $A$ is the area of injection. Since $Q/A$ is the nominal injection velocity normal to the plate, $C_q$ is the ratio of normal to streamwise velocities. However, the area of injection is shown by Madavan et al. (1984) not to be very significant, but rather the ratio of air volume to total volume in the boundary layer

$$C_v = \frac{Q_a}{Q_a + Q_w}, \tag{2.4}$$

where

$$Q_w = U_\infty(\delta - \delta^*)b, \tag{2.5}$$

$\delta^*$ is the displacement thickness, and $b$ is the width of the injection section. In fact, all of the friction ratio data in Madavan et al. (1985a) is presented with the air flow rate nondimensionalized according to (2.4). The debate on proper scaling of MBDR continues, with Sanders et al. (2006) and Elbing et al. (2008) discussing many possible scalings. Given the complexity and number of mechanisms for friction reduction active in this flow, it is unlikely that any simple scaling will adequately collapse the data from different experimental facilities, as noted by Merkle & Deutsch (1992).

The first flat-plate microbubble drag reduction studies in the United States were conducted by Madavan et al. (1984). The experiments were conducted in a rectangular test section with dimensions of 508 mm width × 114 mm height × 762 mm streamwise length. The experimental setup consisted of a 178 mm long porous, sintered stainless steel plate used to inject microbubbles, followed by a 254 mm long drag balance used to measure the integrated skin friction. Figure 2.3 is a schematic of the experimental setup. Madavan et al. (1984) report that "The sintered stainless-steel section is manufactured by Mott Metallurgical Corp. for use as a filter. The filter type chosen will trap particles of diameter 0.5 $\mu$m and larger. The corresponds to a nominal pore size of about 5.0 $\mu$m." This configuration is used for the simulations of Chapter 4, and is the basis for validation of the numerical model presented in Chapter 3. Both the porous section and drag balance have a width of 102 mm and are centered along the test wall centerline. The apparatus was run in three configurations: on the bottom of the test section, on the side and on the top, to explore the effect of gravitational orientation.

Madavan et al. (1984) ran the water tunnel at several speeds and multiple gas injection rates. Tunnel velocities run between 4.2 and 17.4 m/s correspond to length Reynolds numbers between 2.2 and 10.6 million at the downstream edge of the force balance, and 0.7 to 3.0 million at the upstream end of the porous section. The importance of these particular Reynolds numbers is that the boundary layer was fully turbulent before the injection of gas and over the entire porous and drag balance sections. Volumetric airflow rates up to $5 \times 10^{-3}$ $m^3/s$ were used (Madavan et al., 1984). Some of the results of these experiments are replotted in Figure 2.4 and are used later for validation of the numerical model. These results can be collapsed onto one curve by nondimensionalizing the flow rate according to (2.3), as shown in Figure 2.5, which demonstrates the effectiveness of this nondimensionalization for this particular geometry.

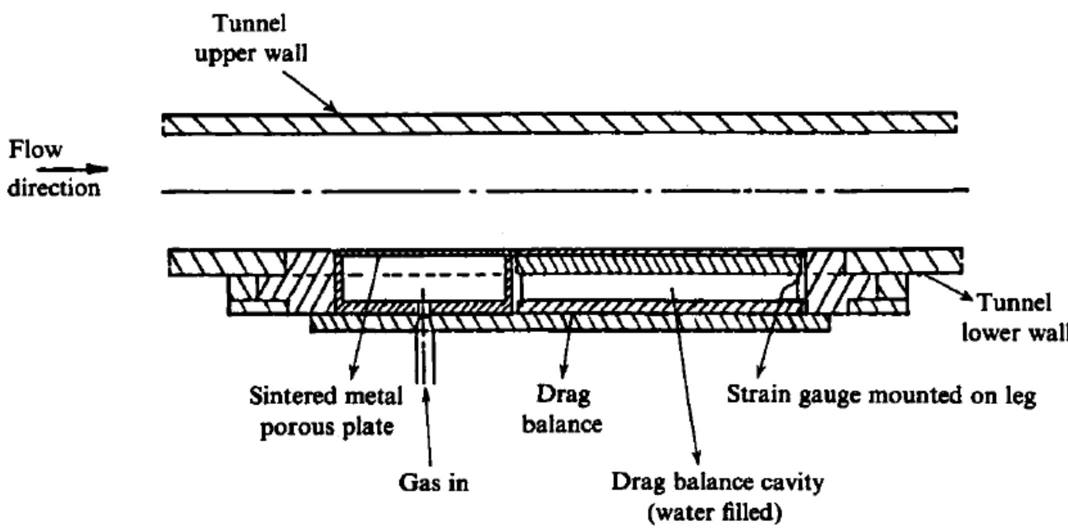


**Figure 2.3.** Schematic of experimental setup showing porous section and force balance. (Madavan et al., 1985a)

The conclusions reached by Madavan et al. (1984) concern the correlation between experimental conditions and the amount of drag reduction measured. First, the volumetric concentration, and not mass concentration of bubbles is the important parameter. This was found by injecting helium in some experiments, where similarity in drag reduction between air and helium injection results was found on the basis of volumetric injection rate, not mass injection rate. Second, by injecting gas through only the downstream half of the porous plate it was shown that the total volumetric air flow rate is important, not the area of injection. Third, buoyancy effects are present. Lower drag values were measured when the plate was placed on the top of the test section. In this configuration, gravity tended to keep the microbubbles close to the plate surface. When the plate was placed on the bottom, gravity tended to pull the bubbles away from the plate surface, leading to slightly higher drag values at the same conditions.

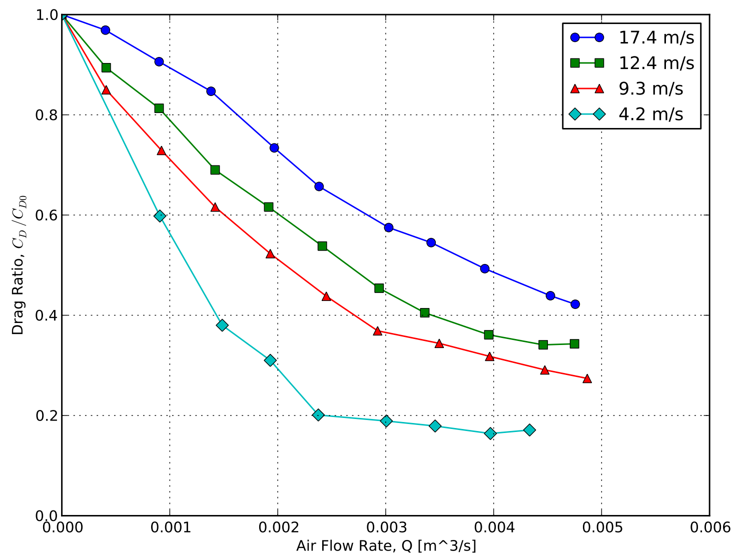


**Figure 2.4.** Experimental drag ratio vs. airflow rate in twelve-inch rectangular tunnel, plate above boundary layer. (Madavan et al., 1984)

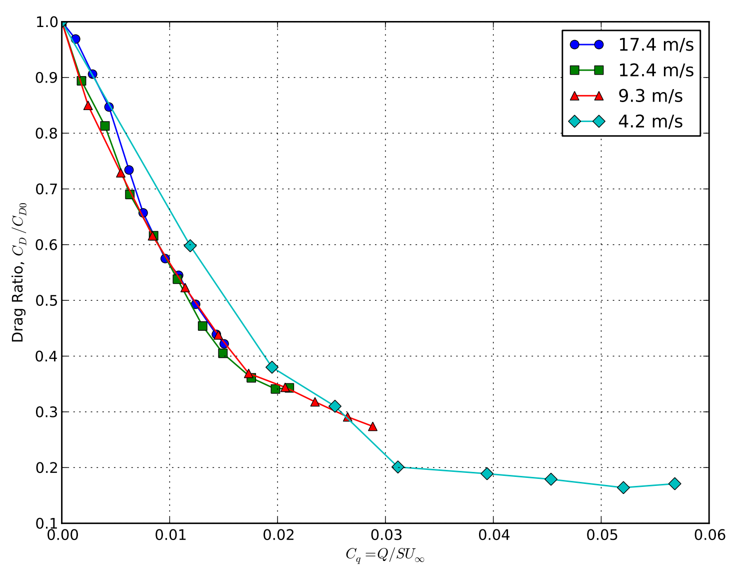


**Figure 2.5.** Experimental drag ratio vs. $C_q$ in twelve-inch rectangular tunnel, plate above boundary layer. (Madavan et al., 1984)

Madavan et al. (1984) also discussed the origin of the drag reduction. The authors argued that the drag reduction, at least at the gas injection rates in their experiments, was not due to boundary layer separation. Boundary layer separation can be caused by an adverse pressure gradient, removal of streamwise momentum or the addition of normal momentum. Pressure taps along the test section showed almost zero streamwise pressure gradient when the gas was turned off and also when gas was being injected. Since gas was injected normal to the mean flow, the potential existed to "blow off" the boundary layer by the addition of normal momentum. However, the authors stated that "The injected air does add momentum, but its level is more than three orders of magnitude less than that required to separate a boundary layer." They added: "there is no mechanism whereby streamwise momentum can be removed from the flow; there is no place for a force to act." The microbubbles in the flow serve for effective visualization. Based on this visual evidence the authors stated: "Every visual evidence is that the microbubble boundary layer remains strongly attached and flat-plate-like in character."

Having ruled out partial or full separation as the cause for the drag reduction, another explanation was postulated. Madavan et al. (1984) believed the hypothesis developed by Lumley (1973) for the drag-reducing effect of polymers in turbulent flows could also explain the drag-reducing effect observed with microbubble injection. Madavan et al. (1984) explain:

> Outside the viscous sublayer of a high Reynolds number turbulent boundary layer, the rotation and strain rate fields are uncorrelated. Polymer molecules found there will stretch, resulting in increased solution viscosity. This additional viscosity (or decreased Reynolds number) will increase the size of the smallest eddies capable of surviving. Just outside the sublayer (the buffer region) where Reynolds stress-producing eddies are roughly the size of the Kolmogorov eddies, the turbulence is dissipated. The sublayer thickness increases and the skin friction is reduced. The same case can be made for certain types of particles in the flow.
>
> In the case of microbubble injection, the viscosity in the sublayer is unaffected because of the absence of bubbles there. Outside this region the bubbles cause both an increase in the absolute viscosity through an Einstein-type relation (say) and a decrease in the solution density. Again, this results in a thicker sublayer. The suggested mechanism offers a path whereby sizable skin friction reductions can be realized without postulating the presence of separation.

In Lumley (1973), he explains his theory of polymer drag reduction. The change in mixture density and viscosity alluded to above will be more throughly examined later, and forms the basis for some analytic approaches to this problem. These ideas are explored quantitatively in an examination of the Kolmogorov microscales of turbulence in Appendix A. The changes in mixture density and viscosity are used to show that the smallest scales of turbulence are lost, as suggested by Lumley.

Madavan et al. (1985a) also made local measurements of skin friction on the same apparatus by means of six hot film probes mounted on the plate surface. Five films were mounted on the force balance, while one was mounted 10 mm upstream of the porous section to check for upstream effects of air injection; air injection was found to have no upstream effect on the flow. Figure 2.6 shows the measured friction ratio downstream of injection at four nondimensional gas flow rates and with the plate placed above (solid lines) and below (dashed lines) the boundary layer. The friction ratio at any location decreases as more gas is added (progressing from curves A to D). Also, the reduction in skin friction is seen to persist longer when the plate is above the boundary layer. This demonstrates the buoyancy effect on friction reduction, which is stronger at lower speeds. However, the friction ratio becomes unity far downstream of injection regardless of the plate orientation. Thus, with the plate on top the friction reduction can be maintained for a longer distance, but eventually the near-wall region is depleted of microbubbles. When this happens the local skin friction returns to the no-injection value.

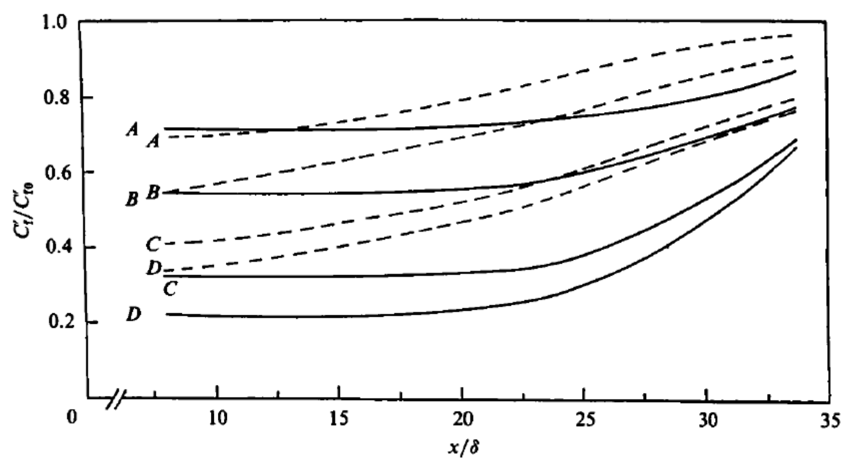


**Figure 2.6.** Downstream persistence of the skin-friction reduction at $U_\infty = 10.7$ m/s. Solid lines: plate on top, dashed lines: plate on bottom. $C_v$ is 0.17 for A, 0.24 for B, 0.34 for C and 0.39 for D. (Madavan et al., 1985a)

The other major finding of Madavan et al. (1985a) is the reduction of high-frequency content in the turbulent fluctuations of shear stress as progressively more gas is injected. Making use of the high temporal resolution of the hot film probes, a spectral analysis of the hot film signals was conducted, leading the authors to conclude “In the presence of microbubbles, the hot-film signals exhibit a reduced high-frequency content and the turbulence energy appears to shift toward lower frequencies.” To determine the effect the porous material on friction reduction, materials with the pore sizes of 0.5 and 100 $\mu$m were used. The authors conclude “Contrary to earlier Soviet results, injection pore size was found to have no major effect on the amount of skin-friction reduction.”

Sanders et al. (2006) conducted microbubble drag reduction experiments at a much larger facility than used in previous experiments. Experiments were conducted on a 3 m wide by 12.9 m long model. Air was injected beneath the test surface, leading to a plate on top configuration. In line with previous findings, a bubble-free layer next to model surface was found at high speeds

(12 and 18 m/s), while an air layer could form on the model surface at a lower speed (6 m/s) and high injection rates. Simple force balance ratios between lift, drag and buoyancy are presented, suggesting that an air layer can form on the test surface if buoyancy is strong enough to overcome the lift and drag forces on individual bubbles.

Elbing et al. (2008) continued work on the same apparatus, and specifically explored the regime where the surface is covered with air, and named it Air-Layer Drag Reduction (ALDR). In the microbubble drag reduction regime, it was found that "significant drag reduction ( > 25%) is limited to the first few meters downstream of injection." This finding is consistent with prior experimental work where the skin friction returns to its no-injection value after a short distance. Concerning air-layer drag reduction, the authors report that "there are three distinct regions associated with drag reduction with air injection: Region I, BDR; Region II, transition between BDR and ALDR; and Region III, ALDR." Once an air layer is established, it can persist the entire length of the model downstream of injection, with drag reduction in excess of 80% for this entire region. The work is most concerned with determining the onset and stability of the ALDR regime.

Fontaine & Deutsch (1992) performed water tunnel experiments on an axisymmetric body to determine if a density effect was present. Gases covering a wide range of densities and solubilities were tested. The density ratio of the heaviest gas, sulfur-hexafluoride, to the lightest, helium, is 39. The authors conclude that "It is conceivable, but unlikely that gas density plays a major role in the drag reduction phenomenon." It was also found that all the gases tested were effective drag reducers, and gas solubility in water is not a significant factor in drag reduction.

## 2.3 Analytic models

Legner (1984) put forth the first analytical model of microbubble drag reduction. He developed a simple stress model to examine the ratio of the total stress in a TBL with microbubbles to the stress in the corresponding flow without microbubbles. The fluid stress in a 2D, turbulent flow is given as

$$\tau = (\mu + \rho q \Lambda)\frac{\partial \bar{u}}{\partial y}, \tag{2.6}$$

where both the viscous and turbulent viscosities are retained. The turbulent velocity is $q$, the square root of the turbulent energy, and $\Lambda$ is the size of the energy-containing eddies for an eddy viscosity description of the turbulence. $\rho$ and $\mu$ denote the liquid density and molecular viscosity, respectively, while $\bar{u}$ is the time-averaged streamwise velocity. Using the subscript $_1$ to refer to the case with microbubbles and no subscript to refer to the single phase case, Legner finds the stress ratio to be

$$\frac{\tau_1}{\tau} = \frac{(\mu_1/\mu + \rho_1 q \Lambda_1/\mu)(\partial \bar{u}/\partial y)_1}{(1 + \rho q \Lambda/\mu)(\partial \bar{u}/\partial y)}. \tag{2.7}$$

The key assumption of this model is that the near-wall velocity gradient is unchanged by the presence of bubbles, which is not strictly true, given the Soviet work discussed by Merkle &

Deutsch (1992). With the contribution of air to the mixture density neglected, along with the contribution of the molecular viscosity in the singlephase case, the stress ratio becomes

$$\frac{\tau_1}{\tau} = \frac{\mu_1/\mu}{\rho q\Lambda/\mu} + (1-\alpha)\frac{q_1\Lambda_1}{q\Lambda}, \tag{2.8}$$

where $\alpha$ is the gas volume fraction. The singlephase eddy viscosity ratio, $\rho q\Lambda/\mu$, is assigned a typical value of 1000, although this value clearly varies through the boundary layer and becomes zero at the wall where the fluctuations vanish. For the molecular viscosity of the mixture, Legner uses the formula of Sibree (1934), developed from measurements of a froth,

$$\frac{\mu_1}{\mu} = \frac{1}{1-1.09\alpha^{1/3}}. \tag{2.9}$$

Applying the singlephase eddy viscosity ratio estimate $\rho q\Lambda/\mu = 1000$ and (2.9) to (2.8) gives

$$\frac{\tau_1}{\tau} = \underbrace{10^{-3}\left(\frac{1}{1-1.09\alpha^{1/3}}\right)}_{\text{viscosity}} + \underbrace{(1-\alpha)\frac{q_1\Lambda_1}{q\Lambda}}_{\text{density-turbulence}}. \tag{2.10}$$

The first term in (2.10) is the viscosity term, while the second is the density-turbulence term. If no account of the turbulence modification is made, then $q_1\Lambda_1/q\Lambda = 1$. By inspection, (2.10) will predict an almost linear reduction in skin friction with increasing $\alpha$ at low gas fractions, as the viscosity term will be negligible given its coefficient of $10^{-3}$. However, the viscosity term rises sharply as $\alpha$ approaches 0.77, where (2.9) is discontinuous. Legner models the turbulence modification by considering the bulk viscosity,

$$\frac{q_1\Lambda_1}{q\Lambda} = \frac{1-\alpha}{\alpha_{\text{lim}}}, \tag{2.11}$$

where $\alpha_{\text{lim}} = 0.8$ is the limiting packing fraction of the bubbles. Substituting this bulk viscosity effect into (2.11) gives Legner's final form for the stress ratio,

$$\frac{\tau_1}{\tau} = 10^{-3}\left(\frac{1}{1-1.09\alpha^{1/3}}\right) + \frac{(1-\alpha)^2}{\alpha_{\text{lim}}}. \tag{2.12}$$

The physical mechanisms of mixture density reduction, viscosity increase, and turbulence modification each appear as distinct mathematical terms in (2.10). This not only brings the mechanisms together in a conceptually pleasing way, but also demonstrates that the relative strengths of the three major mechanisms change greatly with void fraction. As noted, the density effect is dominant as gas fraction increases from zero. However, the increasing mixture viscosity and turbulence modification only become dominant as gas fraction exceeds 0.6. The preceeding review of experimental literature consistently reports minimum skin friction ratios of 0.1 – 0.2. This is consistent with Legner's model, which predicts a lower limit to the friction ratio at high gas fractions.

Interestingly, (2.10) and (2.12) are independent of spatial location $(x, y)$ relative to injection. Legner defines $\alpha$ as the maximum gas concentration in the boundary layer; however, it can be interpreted more generally as the local gas fraction, $\alpha = \alpha(x, y)$ throughout the boundary layer. So, Legner's stress model can be combined with another method to determine $\alpha(x, y)$, e.g. a numerical method. This opens the possibility of combining Legner's stress model with computational fluid dynamics (CFD) for prediction of the entire flow field, including $\alpha(x, y)$ at all points in the domain. Hence, ideas from Legner's model should be incorporated into a turbulence model for MBDR, since it specifically deals with the effect of microbubbles on the stress in the TBL flow.

Marie (1987) developed an analytical model for the skin friction ratio based on Lumley's work. Lumley (1973) argued that microbubbles cause changes in the buffer layer of the boundary layer leading to an increase in sublayer thickness. A comparison is made between the largest (energy-containing) and smallest (dissipative) scales of turbulence. Legner has shown that the presence of the bubbles increases the mixture kinematic viscosity. Marie uses this to show that the peak in viscous dissipation shifts upward from the wall, while the scaling for the largest eddies does not change. Thus, the sublayer thickens, leading to a reduced velocity gradient at the wall, and thus reduced skin friction. This model finds good agreement with skin friction measurements of Madavan et al. (1985a). The greatest shortcoming of this model, however, is that it predicts the skin friction ratio at a single location, the junction of the porous section and the smooth surface that follows it.

Meng & Uhlman (1998) consider the formation of bubbles in a turbulent boundary layer. This is done by evaluating the force balances that prevail at a single pore between surface tension, drag and lift forces. Figure 2.7 shows a schematic of a bubble forming from a pore in still water (left), and one forming in a flowing liquid (right), showing the direction of forces acting on the bubble as it forms. By using reasonable estimates for these forces, different bubble formation regimes are delineated on the basis of a single parameter, the injection coefficient per pore, $v_{\mathrm{pore}}/U_\infty$, where $v_{\mathrm{pore}}$ is the air velocity out of a single pore. Naturally different bubble sizes are produced in the different formation regimes. A theory for drag reduction based on bubble splitting is presented, whereby turbulent energy is expended in the splitting of bubbles. The authors hypothesize that "bubble splitting is a plausible basic mechanism for reducing turbulence in a microbubble-laden turbulent boundary layer." An interesting discussion is made of the significant differences between fresh water and sea water in supporting bubbles. Seawater supports smaller bubbles than fresh water, where bubbles of the same size would quickly coalesce and rise to the surface. This is important if water tunnel tests are used as the basis for design of maritime drag reduction technologies.

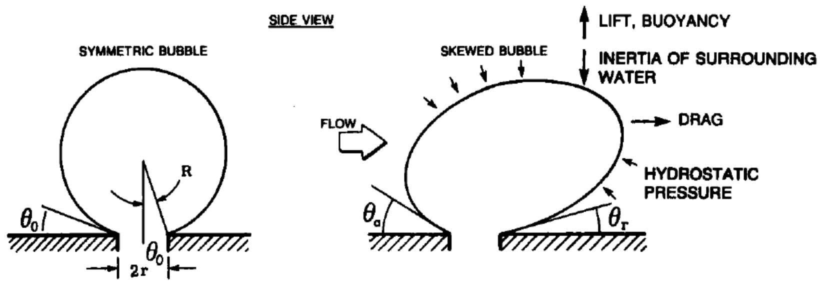


**Figure 2.7.** Bubble formation geometry and nomenclature in static and flowing environments. (Meng & Uhlman, 1998)

## 2.4 Numerical models

The first numerical modeling effort was made by Madavan et al. (1985b), who applied their experimental findings directly to the model they developed. Like Legner (1984), the authors recognized that the microbubbles can affect the turbulence through changing material properties, e.g. density and viscosity, and through direct interaction with the turbulent structure. To avoid the difficulties of turbulence modeling, only the changing material properties are incorporated into the model. The mixture density is

$$\rho_m = (1 - \alpha)\rho_0 + \alpha\rho_g. \tag{2.13}$$

Subscripts m, 0 and g refer to properties of the mixture, liquid and gas, respectively. Two different relations for the mixture viscosity as a function of gas fraction were used. Madavan et al. (1985b) report a model developed by Einstein for very low concentrations of the dispersed (gas) phase, but applied to much higher concentrations,

$$\mu_m = (1 + 2.5\alpha)\mu_0. \tag{2.14}$$

The model due to Sibree, (2.9) is also used. The relative viscosity predicted by the two relations are plotted in Figure 2.8. Both models lead to increasing mixture viscosity with gas fraction, and the Sibree model predicts a much sharper rise in mixture viscosity than Einstein's, becoming discontinuous at $\alpha = 0.772$.

A compressible boundary layer numerical method accepting an arbitrary equation of state and using a mixing length model for turbulence was used to carry out the calculations. After fully-turbulent flow had been established in the model, a predetermined gas fraction profile was imposed over a finite distance, simulating air injection. Such an imposed trapezoidal gas concentration profile is shown in Figure 2.9, which provides the necessary equation of state through property relations (2.13), and (2.14) or (2.9). The left pane shows the imposed gas volume fraction ($\phi$) as a function of height from wall (given in terms of $y^+$ values), while the

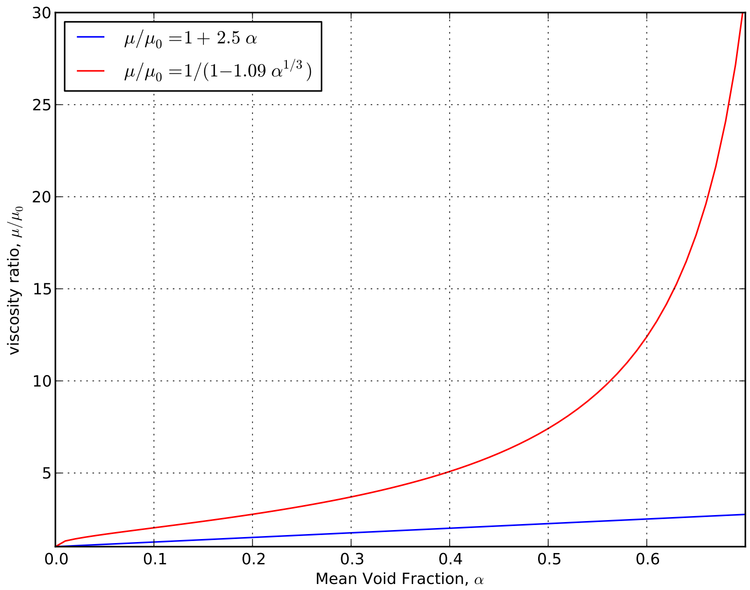


**Figure 2.8.** Ratio of mixture to liquid molecular viscosity as a function of gas fraction, Einstein (blue) and Sibree (red).

next two panes show the resulting mixture properties, normalized by liquid properties. Mixture density ($\rho/\rho_l$) decreases while molecular viscosity markedly increases ($\mu/\mu_l$). The last pane shows the maximum eddy viscosity ratio ($\mu_e/\mu$) to shift further from the wall (Einstein viscosity) or shift away from the wall and increase in magnitude (Sibree viscosity) with microbubbles. Parametric studies of the effect of the height of the bubble cloud on skin friction were carried out, varying the height ($y^+$) of the four vertices of gas concentration profile. These studies showed the boundary layer model to be very sensitive to the location of the inner leg of the profile, and much less so to the location of the outer leg. The optimum inner leg location, resulting in the lowest friction values, is between $y^+ = 10$ to 20 (zero to maximum gas concentration over this distance), which means that bubbles are present in the buffer region but not the sublayer. When gas is present closer to the wall, skin friction increases from the minimum value, because increased mixture viscosity contributes to the skin friction. A maximum gas fraction of 0.5 was used for most of the cases. Computations showed skin friction reductions up to 50%. The most important finding is the importance of the location of the bubbles in the boundary layer; they are most effective when present in the buffer layer, and quickly become less effective as they move further from the wall (Madavan et al., 1985b).

A more sophisticated computational approach to microbubble drag reduction was taken by Kunz et al. (2003). The authors summarize the approach: "An ensemble averaged, multi-field, two-fluid baseline differential model is employed. Interfacial dynamics models are incorporated to

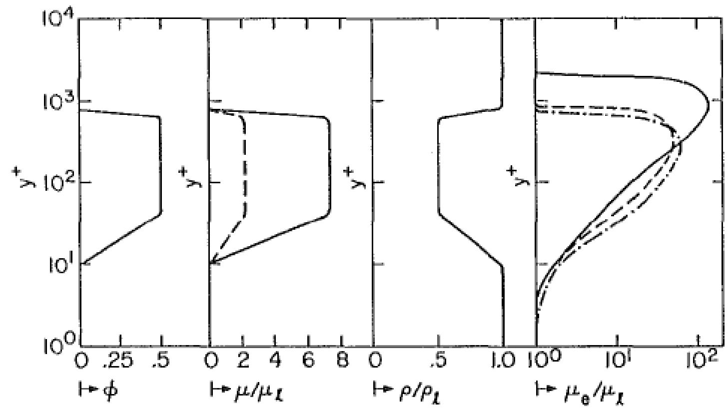


**Fig. 2 Variation of viscosity, density and effective viscosity in the boundary layer for a typical trapezoidal air concentration distribution: _·_·_·, no air case; ____, Sibree model; _ _ _, Einstein model**

**Figure 2.9.** Imposed gas fraction profile and resultant viscosity and density variations. (Madavan et al., 1985b)

account for drag, lift, virtual mass and dispersion. Wall kinematic constraints, porous-wall shear apportionment, coalescence, breakup and attendant turbulence attenuation are also accounted for." A multiphase extension of Menter's sublayer-resolved turbulence model, which is a hybrid k–$\epsilon$/k–$\omega$ model, is applied only to the liquid field. Since the changes to the buffer region are very important, a low Reynolds correction is applied to the turbulence model, and meshes resolving the viscous sublayer are employed.

Turbulence attenuation is captured in the model by incorporating the analysis of Meng & Uhlman (1998) in estimating the turbulent energy extracted in bubble splitting events. This requires further estimates of collision frequency and efficiency. Sink terms in the $k$ and $\omega$ turbulence equations result from bubble splitting, reducing turbulence energy compared to the single phase case. Several bubble size 'bins' are used to represent a continuous range of sizes, and bubble splitting and coalescence leads to mass transfer between bubble fields so that mass is conserved (Kunz et al., 2003).

The model was compared with the force balance measurements presented in Madavan et al. (1984). Computed velocity profiles in inner variables at several gas injection rates are shown in Figure 2.10. A progressive thickening of the sublayer with increasing gas injection is seen. Figure 2.11 shows the computed drag of several multi-fluid simulations (NPHASE, bubble diameter given) and two homogeneous multiphase simulations (UNCLE-M and NPHASE, homogeneous). These results are presented with the nondimensionalized data, and show reasonable agreement, although the multi-field simulations generally predict lower drag than the experiments and homogeneous models predict somewhat higher drag than experiments.

Continued development and validation of this model is presented in Kunz et al. (2007), where the microbubble drag reduction data of Sanders et al. (2006), at much higher Reynolds num-

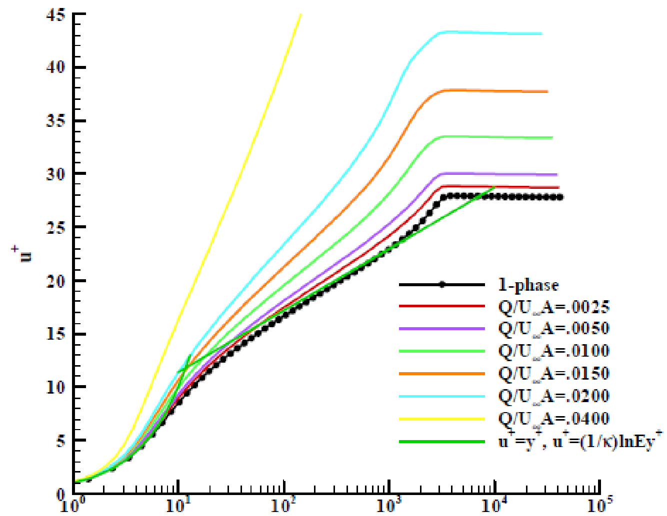


**Figure 2.10.** Predicted boundary layer velocity profiles, in inner variables, for experiments of Madavan et al. (Kunz et al., 2003)

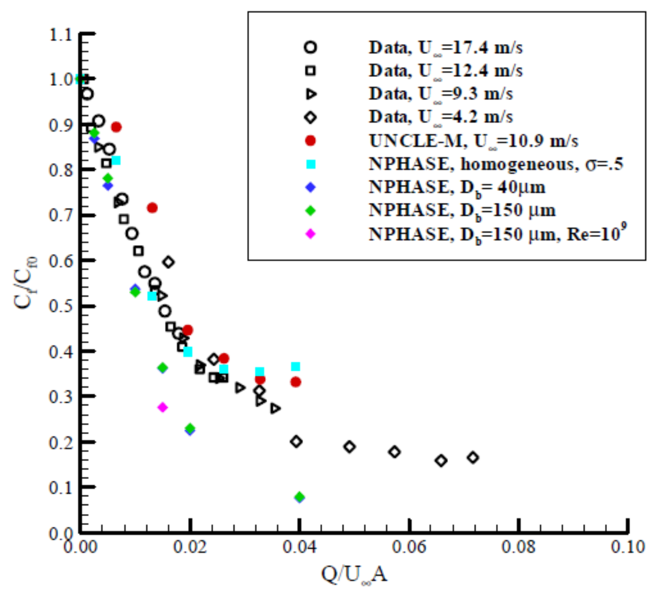


**Figure 2.11.** Predicted and measured drag ratio vs. nondimensional flow rate, for experiments of Madavan, et al. (Kunz et al., 2003)

bers than Madavan et al. (1984), is used for validation. The model is also compared to Direct Numerical Simulations (DNS) of fully-developed channel flow with bubbles. These comparisons "demonstrate the importance of collision-induced bubble dispersion compared to conventional homogeneous-turbulence dispersion" (Kunz et al., 2007).

Skudarnov & Lin (2006) conducted a study of the drag ratio effect on the effectiveness of drag reduction by gas injection. The density ratio is the ratio of the liquid density to the gas density. The singlephase, unsteady Reynolds-averaged Navier-Stokes (RANS) model with a species transport equation was used to represent the two-phase, turbulent flow. A standard $k-\omega$ turbulence model with low Reynolds number correction was applied. The local mass fraction of species $i$, $y_i$, is found from solving the convection-diffusion equation

$$\frac{\partial}{\partial t}(\rho\, y_i) + \nabla \cdot (\rho\, \mathbf{u}\, y_i) = -\nabla \cdot \mathbf{J}_i + S_i \tag{2.15}$$

where $\mathbf{J}_i$ is the diffusion flux of species $i$ and $S_i$ is the rate of creation from sources. The diffusive flux is given by

$$\mathbf{J}_i = -\left(\rho D_{i,m} + \frac{\mu_t}{Sc_t}\right)\nabla y_i \tag{2.16}$$

where $Sc_t$ is the turbulent Schmidt number, $\mu_t$ is the turbulent viscosity, and $D_{i,m}$ is the diffusion coefficient for species $i$. The Schmidt number characterizes flows with simultaneous momentum and mass diffusion processes, and is the ratio of molecular momentum diffusivity to molecular mass diffusivity (Incropera et al., 2007). Thus, the turbulent Schmidt number is the ratio of turbulent dispersion of momentum to turbulent dispersion of mass,

$$Sc = \frac{\mu}{\rho D} \tag{2.17a}$$

$$Sc_t = \frac{\mu_t}{\rho D_t}. \tag{2.17b}$$

Mass dispersion of species $i$ by the turbulent motions is estimated in (2.16) from the calculated turbulent viscosity and a prescribed turbulent Schmidt number,

$$\rho D_t = \frac{\mu_t}{Sc_t}. \tag{2.18}$$

Skudarnov & Lin (2006) did not give the value used for $Sc_t$, however they probably follow Kunz in using a value of one.

Skudarnov & Lin (2006) used the experiments of Madavan et al. (1984) for validation of their model. It is unclear why $CO_2$ was chosen for injection, as air was injected in the experiments. Total drag reduction results are in line with those of Kunz et al. (2003), with computations predicting lower drag than the experiments. These simulations showed that a simple homogeneous model can provide reasonable drag reduction results, although this had been established by Madavan et al. (1985b) and Kunz et al. (2003). The figures of Skudarnov & Lin (2006) show changes in drag reduction with density ratio, but only when this ratio changes by orders of magnitude. In effect, this would mean using a range of different gases. For obvious reasons of economy, air is typically used in these experiments, and would likely be used in any actual drag reduction system applied to ships at sea.

## 2.5 Summary

Several physical mechanisms leading to the reduction of drag have been identified. The reduction of the turbulent Reynolds stress $-\rho\,\overline{\mathbf{u'}\otimes\mathbf{u'}}$ through its density dependence is the dominant effect leading to the reduction of local skin friction. Many secondary effects enhance the reduction of skin friction. The increase of kinematic viscosity in the buffer layer was proposed by Madavan et al. (1984) to cause a loss of the smallest scales of turbulence. This concept is further developed in Appendix A. Meng & Uhlman (1998) hypothesize that some turbulent energy is expended in the splitting of bubbles. Finally, Legner (1984) describes a 'bulk compressibility' of the bubbly mixture which can absorb some turbulent energy like a damper. While inclusion of the secondary mechanisms is required for a detailed study of MBDR, they are not necessary when the net change in drag with gas injection is the quantity of interest.

Given the predominance of the density effect in producing drag reduction, a lower-order model is proposed. The homogeneous fluid approach of the model incorporates the locally reduced fluid density through the calculation of volume-weighted fluid properties based on the local volume fractions of air and water at any spatial location. Inclusion of turbulent dispersion leads to mixing of the phases downstream of injection. It is proposed that this formulation, which neglects secondary causes of drag reduction, is sufficient for engineering calculations of total drag on a body supporting a turbulent boundary layer with gas injection. Details of the model are presented in Chapter 3 and simulation results in Chapter 4 demonstrate the validity of this approach.

Chapter 3

# Governing Equations and Multiphase Model

As the literature review of Chapter 2 showed, there are many physical mechanisms acting to cause the microbubble drag reduction effect. However, the decreased mixture density is the main effect, which is captured in a pressure-based, compressible, multiphase model. The secondary effects are not included in this numerical model. We review the general conservation equations governing this flow and assumptions used in development of this model. Equations of state used for the two phases are presented.

The approach to turbulence taken here is the unsteady Reynolds-averaged Navier-Stokes (URANS) approach. URANS models do not resolve the small fluctuations in velocity and pressure characteristic of a turbulent flow. Instead, the larger-scale flow features are resolved, and the effects of turbulent fluctuations appear as an apparent stress in the momentum equation. The averaging process and resulting Reynolds-averaged Navier-Stokes equations are explained by Wilcox (1998).

## 3.1 Governing equations

The two-phase fluid flow is governed by the conservation laws of nature: conservation of mass, momentum and energy. The general, compressible form of conservation of mass, or continuity, is

$$\frac{\partial \rho}{\partial t} + \nabla \cdot (\rho\, \mathbf{u}) = 0, \tag{3.1}$$

where $\rho$ is mixture density, $\mathbf{u}$ is velocity and $\mathbf{x}$ is the spatial Cartesian coordinate. The general form for conservation of momentum (Newton's second law) is

$$\rho \frac{D\mathbf{u}}{Dt} = \rho\, \mathbf{g} + \nabla \cdot \mathbf{T}, \tag{3.2}$$

where the material derivative of a scalar or vector $F$,

$$\frac{DF}{Dt} = \frac{\partial F}{\partial t} + \mathbf{u} \cdot \nabla F, \tag{3.3}$$

is used to describe the total rate of change of a flow variable in an Eulerian description. The fluid behavior is captured in the mathematical description of the Cauchy stress tensor $\mathbf{T}$ of (3.2). The general form for the laminar stress tensor for a Newtonian fluid includes contributions from pressure and the strain rate of the fluid:

$$\mathbf{T}_{\text{laminar}} = -p\,\mathbb{I} + 2\mu\mathbf{D} + \lambda\,(\nabla \cdot \mathbf{u})\,\mathbb{I}, \quad \mathbf{D} = \text{Sym}(\nabla\mathbf{u}). \tag{3.4}$$

$\mu$ and $\lambda$ are the shear and bulk viscosities, respectively. $\lambda$ is known as the bulk viscosity because it is only associated with volumetric expansion or contraction of the fluid. $\mathbb{I}$ is the identity tensor. Stokes' hypothesis is used to eliminate the problem of determining this coefficient:

$$\lambda + \frac{2}{3}\mu = 0. \tag{3.5}$$

With Stokes' hypothesis, (3.4) simplifies to

$$\mathbf{T}_{\text{laminar}} = -p\,\mathbb{I} + 2\mu\left[\mathbf{D} - \frac{1}{3}(\nabla \cdot \mathbf{u})\,\mathbb{I}\right]. \tag{3.6}$$

The linear relation between stress and strain rate in (3.6) specifies the fluid as Newtonian.

The effects of the small-scale turbulence are included in the Reynolds Stress tensor, $-\rho\,\overline{\mathbf{u}' \otimes \mathbf{u}'}$. Adding the Reynolds stress term gives the complete expression for the stress tensor in a turbulent flow:

$$\mathbf{T}_{\text{full}} = -p\,\mathbb{I} + 2\mu\left[\mathbf{D} - \frac{1}{3}(\nabla \cdot \mathbf{u})\,\mathbb{I}\right] - \rho\,\overline{\mathbf{u}' \otimes \mathbf{u}'}. \tag{3.7}$$

Substituting (3.7) into (3.2) gives the unsteady Reynolds-Averaged Navier-Stokes equation:

$$\rho\frac{D\mathbf{u}}{Dt} = \rho\,\mathbf{g} + \nabla \cdot \left\{-p\,\mathbb{I} + 2\mu\left[\mathbf{D} - \frac{1}{3}(\nabla \cdot \mathbf{u})\,\mathbb{I}\right] - \rho\,\overline{\mathbf{u}' \otimes \mathbf{u}'}\right\}. \tag{3.8}$$

The Reynolds Stress tensor is modeled with the Spalart-Allmaras turbulence model throughout this thesis.

## 3.2 Multiphase model

The presentation of the model closely follows that of Miller et al. (2012), the authors of the OpenFOAM-based solver uwlFoam. The authors summarize the handling of the two phase mixture in the model:

> The resulting multi-species model follows the standard homogeneous treatment – interfacial dynamics are neglected under the assumption that there is no slip between

> constituents residing in the same control volume. In fact, through volume averaging, the multiphase mixture can be treated as a single-phase fluid with property values based on averages of the properties of the constituent phases.

Due to control volume averaging only the velocity of the mixture is defined. Material properties are assigned local values based on a local volume fraction. Equations are solved by the numerical model for the volume fraction of the gas, $\alpha_1$, velocity $u$ and pressure $p$ as presented below. The method is also pressure-based, meaning that the phasic densities are determined from the pressure, $\rho_k = \rho_k(p)$.

### 3.2.1 Equations of state

An isentropic gas equation of state (EOS) is used for the phase 1, while a constant speed of sound, compressible, isothermal EOS is applied to phase 2. Since both phases have an isentropic equation of state, the entire system is isentropic. Thus, no differential energy equation needs to be solved.

#### 3.2.1.1 Phase 1: Isentropic gas

Assuming the gas is subject only to isentropic processes leads to the constraint

$$\frac{p}{\rho^\gamma} = a_c, \tag{3.9}$$

where $\gamma$ is the constant ratio of specific heats and $a_c$ is the prescribed isentropic constant. $a_c$ is calculated according to (3.9) from a reference pressure, such as a fixed pressure on the boundary, and the material properties used for the gas. Gas density is then calculated as

$$\rho_1 = \left(\frac{p}{a_c}\right)^{1/\gamma}. \tag{3.10}$$

#### 3.2.1.2 Phase 2: Compressible liquid

The speed of sound in a fluid medium is given by

$$\left.\left(\frac{d\rho}{dp}\right)\right|_s = \frac{1}{c^2}, \tag{3.11}$$

where $c$ is the speed of sound and the derivative is taken at constant entropy. Assuming a constant sound speed, integration of (3.11) yields the liquid state equation

$$\rho_2 - \rho_0 = \frac{1}{c^2}(p - p_0), \tag{3.12}$$

with $\rho_0$ and $p_0$ arising as constants of integration representing a reference density and pressure, respectively, each of which are prescribed. For convenience, the compressibility of phase $k$ is given its own symbol:

$$\psi_k = \frac{\partial \rho_k}{\partial p} = \frac{1}{c^2} \tag{3.13}$$

The mixture density is calculated by volume-weighting the phasic densities as

$$\rho = \alpha_1 \rho_1 + \alpha_2 \rho_2, \tag{3.14}$$

and mixture density is similarly calculated from mixture viscosities as

$$\mu = \alpha_1 \mu_1 + \alpha_2 \mu_2. \tag{3.15}$$

### 3.2.2 Volume fraction equation

The volume fraction equation is derived from the balance of mass for species 1:

$$\frac{\partial}{\partial t}(\alpha_1 \rho_1) + \nabla \cdot (\alpha_1 \rho_1 \mathbf{u}) = 0, \tag{3.16}$$

which is manipulated into a volume fraction equation for phase 1 through application of the chain rule on the derivative of density with respect to pressure:

$$\dot{\alpha}_1 + \mathbf{u} \cdot \nabla \alpha_1 = -\frac{\alpha_1}{\rho_1} \psi_1 (\dot{p} + \mathbf{u} \cdot \nabla p) - \alpha_1 \nabla \cdot \mathbf{u}. \tag{3.17}$$

The volume fraction of liquid, $\alpha_2$, is found from the algebraic constraint

$$\alpha_1 + \alpha_2 = 1. \tag{3.18}$$

### 3.2.3 Pressure equation

As there is no governing relation for the pressure, mass conservation is used to develop a pressure equation. Adding the volume fraction equations for species 1 and 2 we obtain

$$\left( \frac{\alpha_1}{\rho_1} \psi_1 + \frac{\alpha_2}{\rho_2} \psi_2 \right) (\dot{p} + \nabla \cdot p\mathbf{u} - p \, \nabla \cdot \mathbf{u}) + \nabla \cdot \mathbf{u} = 0. \tag{3.19}$$

### 3.2.4 Spalart-Allmaras turbulence model

To model the turbulent stress, $-\rho \overline{u_i\prime u_j\prime}$, the one-equation model developed by Spalart & Allmaras (1994) is used throughout the computations of this thesis. A single transport equation for a turbulence-like scalar, $\tilde{\nu}$, is solved, from which the turbulent viscosity $\nu_t$ is calculated.

### 3.2.5 Turbulent dispersion

The model as formulated disallows mixing between phases. Any mixing that occurs in computations is due to numerical diffusion. To model the bubble cloud in a continuum sense, dispersion of air into the water is necessary, in keeping with experimental findings. A new turbulent diffusion term is added, following the formulation of the species transport equation of Skudarnov & Lin (2006). The mass fraction-based transport model of Skudarnov & Lin is adapted to the volume fraction-based formulation used in this study:

$$\nabla \cdot \left( \frac{\mu_t}{Sc_t} \nabla y_1 \right) \Rightarrow \nabla \cdot \left[ \frac{\mu_t}{Sc_t} \nabla \left( \alpha_1 \frac{\rho_1}{\rho} \right) \right] \tag{3.20}$$

where $y_1$ and $\alpha_1$ are the mass and volume fractions of gas, respectively. This new term causes mixing of the phases, so that the volume fraction of air, which is unity at the injection location, gradually reduces downstream as the air is spread out laterally from the plate.

### 3.2.6 Gas injection model

Air can be added to the domain by specifying a fixed velocity into the domain at the injection location on the boundary and fixing the void fraction at that location to one. Another means of adding air to the domain is using a mass (volume) source term in the volume fraction equation. This is also follows Skudarnov & Lin (2006), who state

> The $CO_2$ gas was introduced as species mass source in the first layer of cells along the porous section of the flat plate.

In order to create a volumetric source term, a **source** vector is introduced, which can be thought of as an additional velocity field that *exists only in the volume fraction equation.* As such, a new advection term appears on the left hand side of the volume fraction equation, which becomes negative when moved to the right hand side. Its only purpose is to act as a source term for air. We can add air to the domain with a prescribed velocity on the injector, with $\alpha_1 = 1$:

$$\dot{V}_{air,\mathbf{u}} = -\int_{injector} \mathbf{u} \cdot \hat{n} \, dS \tag{3.21}$$

Alternatively, we can add air to the domain with the source term:

$$\dot{V}_{air,\mathbf{source}} = -\int_{injector} \mathbf{source} \cdot \hat{n} \, dS \tag{3.22}$$

and we see that the two equations have the same form. At the injector location, a zero-gradient condition on $\alpha_1$ is specified when using the source term. The rationale for introducing a source term, rather than just using a specified velocity, is that no-slip velocity can be maintained on the injector when air is introduced.

### 3.2.7 New volume fraction and pressure equations

After adding the new terms for volumetric source and turbulent dispersion, the new governing equation for the gas volume fraction becomes

$$\begin{aligned}\dot{\alpha}_1 + \mathbf{u}\cdot\nabla\alpha_1 &= -\frac{\alpha_1}{\rho_1}\psi_1\left(\dot{p} + \mathbf{u}\cdot\nabla p\right) - \alpha_1\nabla\cdot\mathbf{u} \\ &- \nabla\cdot(\mathbf{source}) + \frac{1}{\rho_1}\text{div}\left[C_{\text{disp}}\,\mu_T\,\nabla\left(\frac{\alpha_1\rho_1}{\rho}\right)\right],\end{aligned} \tag{3.23}$$

where the dispersion coefficient $C_{\text{disp}}$ is the reciprocal of the turbulent Schmidt number,

$$C_{\text{disp}} = \frac{1}{Sc_t}. \tag{3.24}$$

$C_{\text{disp}}$ is a specified constant in the simulations, and is given a value of one in multiphase simulations unless noted otherwise. Since the pressure equation is formed by adding the two volume fraction equations, the new terms in the gas volume fraction equation become source terms in the new pressure equation

$$\begin{aligned}\left(\frac{\alpha_1}{\rho_1}\psi_1 + \frac{\alpha_2}{\rho_2}\psi_2\right)&\left(\dot{p} + \nabla\cdot p\mathbf{u} - p\,\nabla\cdot\mathbf{u}\right) + \nabla\cdot\mathbf{u} = \\ &- \nabla\cdot(\mathbf{source}) + \frac{1}{\rho_1}\text{div}\left[C_{\text{disp}}\,\mu_T\,\nabla\left(\frac{\alpha_1\rho_1}{\rho}\right)\right].\end{aligned} \tag{3.25}$$

(3.23) and (3.25) are the final forms of the volume fraction and pressure equations, respectively, implemented and used in the computations of the next chapter.

## 3.3 Finite volume method

The equations presented in section 3.2 are solved approximately with the finite volume method, a technique which transforms a set of partial differential equations into a set of algebraic equations. These algebraic equations are solved using a cell-centered finite volume scheme. The basic idea is to integrate a differential equation over a small, finite volume, called a cell. For example, continuity (3.1) can be integrated over a control volume $V$:

$$\int_V \frac{\partial\rho}{\partial t}\,dV + \int_V \nabla\cdot\rho\mathbf{u}\,dV = 0. \tag{3.26}$$

Gauss's theorem is then used to replace the volume integral of $\nabla\cdot\rho\mathbf{u}$ with a surface integral:

$$\frac{\partial}{\partial t}\int_V \rho\,dV + \int_S \rho\mathbf{u}\cdot\mathbf{n}\,dS = 0 \tag{3.27}$$

where $S$ is the surface of the cell and $\mathbf{n}$ is the outward normal. Details of the finite volume method are given by Ferziger & Perić (2002), and include choices for approximating the surface and volume integrals, for example those in (3.27).

A flow solver is constructed from the governing and auxiliary equations using the open-source CFD framework provided by OpenFOAM. Settings used in the simulations of the following chapter are given in Table 3.1, and a full explanation of terms can be found at OpenFOAM (2012). Once the algebraic system of equations is assembled from the discretized equations, it

**Table 3.1.** Numerical schemes used for interpolation and differentiation

| scheme | method |
|---|---|
| **ddtSchemes** | |
| default | Euler |
| **gradSchemes** | |
| default | Gauss linear |
| **divSchemes** | |
| div(rho*phi,U) | Gauss upwind |
| div(source) | Gauss linear |
| div(phi,alpha) | Gauss vanLeer01 |
| div(phirb,alpha) | Gauss interfaceCompression 1 |
| div(phi,pd) | Gauss upwind |
| div(phid,pd) | Gauss upwind |
| div((nuEff*dev(grad(U).T()))) | Gauss linear |
| default | Gauss upwind |
| **laplacianSchemes** | |
| default | Gauss upwind |
| **interpolationSchemes** | |
| default | linear |
| **snGradSchemes** | |
| default | corrected |

must be solved numerically. This step reduces to solving many matrix inversion problems of the type

$$\mathbf{A}\mathbf{x} = \mathbf{b} \tag{3.28}$$

where $\mathbf{A}$ and $\mathbf{b}$ are known, and the system must be solved for $\mathbf{x}$. Since typical CFD problems give rise to large matrix systems, many computationally efficient methods for solving (3.28) have been developed. These methods are known as linear solvers because they solve sets of linear equations, represented by (3.28). Futhermore, these linear solvers do not solve (3.28) exactly, but rather produce solutions which are successively closer to the exact solution, in a number of inner iterations. A tolerance is specified for each linear solver, which indicates how well the linear system is solved. A lower tolerance means the equations are solved more accurately. This is done in the file fvSolution, where settings are specified for each discrete equation that is solved. The tolerances used in the computations of this thesis are given in Table 3.2. All equations are solved with the preconditioned bi-conjugate gradient (PBiCG) solver, and preconditioned with the diagonal incomplete lower upper (DILU) method. More details on linear systems are available at OpenFOAM (2012).

**Table 3.2.** Tolerances on linear equation solvers

| variable | tolerance |
|---|---|
| $p$ | 1e-6 |
| $U$, $\tilde{\nu}$ | 1e-5 |
| $\alpha_1$ | 1e-9 |

## 3.4 Approach to simulations

The model for microbubble drag reduction presented in this chapter is implemented in the open-source CFD environment OpenFOAM. Gas injection and turbulent dispersion are modeled through the addition of terms to the gas volume fraction equation.

The drag ratios reported in the literature are steady values. When drag measurements with gas injection were taken, researchers ensured that the reported values were constant in time. The focus of research was how steady drag values changed with injection, and transient details of the flow were not reported. Similarly, the goal of simulations is to find the drag values with gas injection after all transient effects have disappeared; the steady condition is sought.

The model formulation presented in this chapter is transient due to the presence of the time derivatives in the governing equations for velocity, pressure and gas volume fraction. This transient formulation is not ideal for steady simulations, as it is designed to capture the change in flow properties with time. However, such a transient formulation can be used to solve steady problems when the boundary conditions are steady. The approach here is to run the simulations in time until the solution has reached its steady (unchanging) value.

At each speed, single phase simulations of water flowing over the flat plate with no gas injection are performed. Computed drag on the force balance is monitored, and simulations are only stopped after a steady value for drag has been achieved. These are the baseline simulations to which multiphase simulations are compared, and serve two purposes. First, the steady, single phase drag values $D_0$ from these cases are used to nondimensionalize the drag from multiphase simulations at the same speed according to (2.2). Second, the steady solution fields from these simulations represent the fully-developed TBLs into which gas is injected. The pressure, velocity and turbulence fields from these steady simulations are used as the initial conditions for multiphase simulations at the same speed.

Multiphase simulations were run out until a steady drag values $D$ were established just as in the single phase simulations. However, convergence of multiphase simulations took much longer than single phase, both in physical time and computational (wall) time. In transient simulations the time step size $\Delta t$ depends on both the local velocities and mesh spacings in the grid. Specifically, small time steps are required when velocities are high, or even modest, in areas of high mesh concentration. This is the case in these simulations; gas injection at the wall causes flow normal to the wall at the injection location. This in turn leads to small time steps, and long computer run times to convergence. Despite this difficulty, simulations were carried out until convergence of $D$ was reached, ensuring that reported values for drag ratio are steady.

Chapter 4

# Computations

## 4.1 Single phase validation

The simulations in this section show that the numerical model captures the important features of a single phase, turbulent boundary layer of water. The simulations model the experiments and geometry of Madavan, Deutsch, and Merkle in the twelve-inch water tunnel at The Pennsylvania State University's Applied Research Laboratory (Madavan et al., 1984).

Two-dimensional simulations are performed in the midplane of the rectangular test section. As the the experiments occur just downstream of a honeycomb to remove turbulence, the two-dimensional computations are justified as long as test section blockage from the boundary layers on the sides is small compared to tunnel width. This simplification greatly reduces computational expense and is in keeping with the computational efforts in the literature of this experimental setup (Kunz et al., 2003; Skudarnov & Lin, 2006). The primary metrics for single phase validation are matching skin friction curves $C_f(Re_x)$, and velocity profiles $u(y)$, between simulations and established correlations.

### 4.1.1 Computational domain

The computational domain corresponds to the experimental setup described in Madavan et al. (1984) where drag with microbubble injection was measured. The naturally-developed TBL on the tunnel wall was used in the experiments. The virtual origin of this TBL was established 180 mm upstream of the beginning of the injection (porous) section by examining $\delta^\star$ and $\theta$, the displacement and momentum thicknesses, respectively of the TBL at several downstream locations. Since $\delta^\star$ and $\theta$ both grow with distance from the virtual origin to the 4/5 power, the virtual origin itself is linearly extrapolated from a plot of $\delta^{\star 5/4}$ and $\theta^{5/4}$. This plot is given by Figure 4.1.

The regions of the computational domain are shown in Figure 4.2, which also shows the mesh. In order for the computational domain to reflect the experiments, the 'leading plate' patch in the simulation has length of 0.180 m, in accordance with the virtual origin determination above. The injector patch is 0.178 m long, and the force balance is 0.254 m long. The test section height is 0.114 m.

### 4.1.2 Boundary conditions and material properties

A constant velocity $U_\infty$ to the right is imposed at the inlet on the left, while the no slip condition is imposed with fixed zero velocity on the bottom of the domain. The average pressure at the outlet is specified as $p_{outlet} = p_{atm} = 101{,}325$ Pa, while a zero-gradient condition on pressure is used on all other patches. On the top, a slip condition is imposed on velocity, meaning that no flow is allowed through the surface ($v = 0$), and a zero-gradient condition is imposed on the tangential component of velocity, $\partial u/\partial y = 0$. The assumption underlying the use of the slip condition at the top is that the boundary layer on the opposite wall can be neglected. The primary effect of the neglected boundary layer is a displacement outward of the effective wall location, leading to a mildly accelerating freestream velocity. The turbulence variable $\tilde{\nu}$ is fixed at the inlet to $5 \times 10^{-7}$ m$^2$/s, is fixed to 0 along the bottom three patches, and is assigned a zero normal gradient condition elsewhere. The turbulent viscosity vanishes at the no-slip wall as the fluctuations vanish approaching the wall.

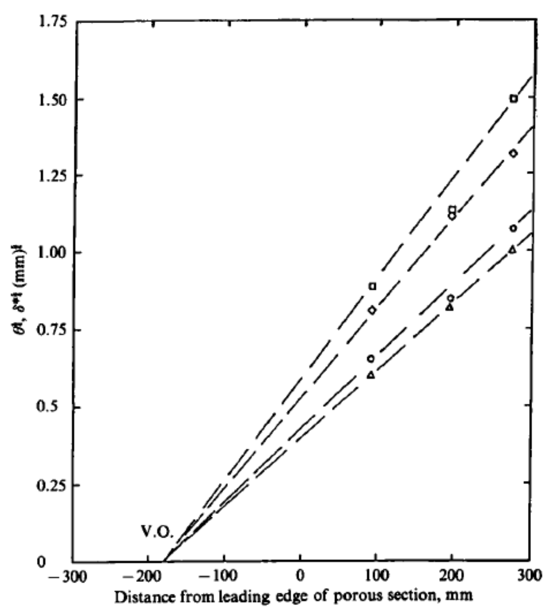


**FIGURE 5.** Determination of the virtual origin: □, $\delta^*$ values, $U_\infty = 4.7$ m/s; ◇, $\delta^*$ values, $U_\infty = 10.6$ m/s; ○, $\theta$ values, $U_\infty = 4.7$ m/s; △, $\theta$ values, $U_\infty = 10.6$ m/s.

**Figure 4.1.** Determination of virtual origin of the turbulent boundary layer which forms naturally on the test-section wall (Madavan et al., 1985a).

The material properties used for water in the single phase (and multiphase) simulations are given in Table 4.1.

**Table 4.1.** Water properties specified for single phase simulations

| symbol | variable | value | units |
|---|---|---|---|
| $\nu_l$ | kinematic viscosity | $1.0 \times 10^{-6}$ | $m^2/s$ |
| $\rho_{0,l}$ | reference density | 1000 | $kg/m^3$ |
| $p_0$ | reference pressure | 101325 | Pa |
| $\psi_2$ | water compressibility | $4.4 \times 10^{-7}$ | $s^2/m^2$ |
| $T$ | water temperature | 288 | K |
| $C_{\text{disp}}$ | dispersion coefficient | 0 | – |

### 4.1.3 Computational mesh

The mesh used in computations must be fine enough to resolve the sharp velocity gradients at the no-slip wall along the bottom, and also have enough streamwise resolution to capture the changes with downstream distance in both single phase and multiphase flow. The mesh used for all cases is shown in Figure 4.2. Note the highly refined mesh near the bottom surface and the axial clustering at the leading and trailing edges of the mesh and at the junctions between the leading plate, injector (porous plate) and force balance patches. The mesh near-wall spacing requirement

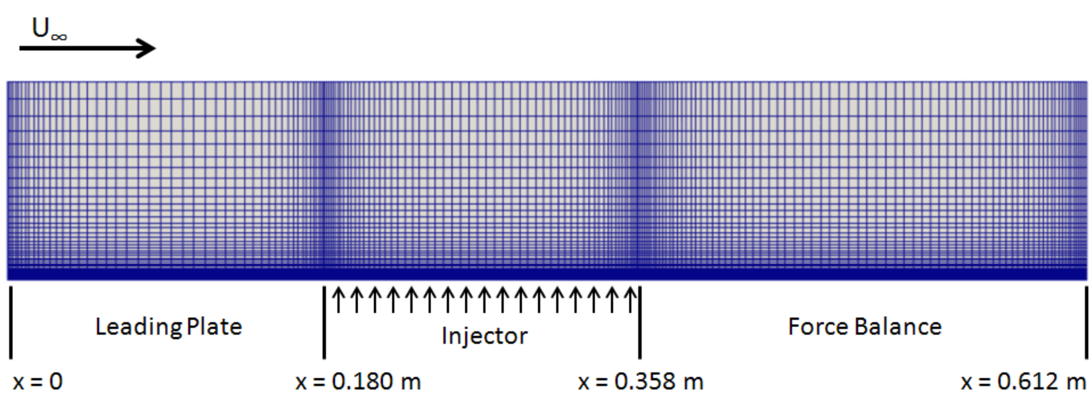


**Figure 4.2.** Numerical grid used in computations, showing: upstream region (Leading Plate); porous injection region (Injector); and location of the floating drag balance (Force Balance). Gas injection is indicated by small arrows. Flow is from left to right over flat plate sections.

is determined by the approach taken with regard to the numerical boundary condition provided to the flow solution at the wall in the turbulent boundary layer. The approach here does not use wall functions, so a 'sublayer mesh' must be used, which requires very short cells close to the wall that reach the viscous sublayer. This approach requires many more cells than the wall function approach, but is recommended by Kunz et al. (2003) because of the important changes in the buffer layer which are not resolved by the wall function approach. Near-wall grid spacing is derived by Boger (2004) from a flat plate correlation, where $\Delta y_1$ is the height of the first cell from the surface and $y^+_{cc}$ is the $y^+$ value specified at the cell center, to be

$$\Delta y_1 = 14\, y^+_{cc}\, Re_L^{-13/14} L. \tag{4.1}$$

The same mesh is used at different speeds and the near-wall spacing is governed by the highest speed, 17.4 m/s. Evaluating (4.1) at $U_\infty = 17.4$ m/s and using the material and geometric properties of the flow give $\Delta y_1 = 2.55 \times 10^{-6}$ m when $y^+_{cc} = 1$. This height is applied to the first cell, and a geometric growth rate of 1.1 is used normal to the wall, so that resolution gradually decreases away from the wall where it is not needed. Because a slip condition is applied at the top, no boundary layer exists there (the fluid slips along the top), high resolution is not needed. This reduces the computational resources needed to compute the flow solution.

187 streamwise by 87 wall normal cells are used for a total of 16,456 cells. This is much denser than the $96 \times 64$ cells used by Kunz et al. (2003) or the $113 \times 65$ cells used by Skudarnov & Lin (2006) for the same geometry.

### 4.1.4 Single phase simulations

Single phase simulations are performed at the three free stream speeds given in Table 4.2. The Reynolds number based on total plate length, $Re_L = U_\infty L/\nu$ is also given, where $L = 0.612$ m is the length from the virtual origin (beginning of computational domain) to the end of the force balance.

**Table 4.2.** Free stream speeds and corresponding Reynolds numbers for single phase simulations

| $U_\infty$ [m/s] | $Re_L$ |
|---|---|
| 9.3 | $5.69 \times 10^6$ |
| 12.4 | $7.59 \times 10^6$ |
| 17.4 | $1.06 \times 10^7$ |

### 4.1.5 Single phase velocity profiles

Representative validation results are presented at 12.4 m/s. The streamwise velocity profiles normal to the plate, $u(y)$, are shown in Figure 4.3 with a common origin. The growth of the boundary layer clearly can be seen with increasing $x$. These velocity profiles can be presented in 'outer variables', meaning that the velocity and distance from the wall are nondimensionalized using scales representative of the large scales characteristic of the outer edge of the boundary layer. These outer scales are the boundary layer thickness $\delta$ and velocity prevaling at the edge of the boundary layer, $U_{\text{edge}}$. Figure 4.4 presents the velocity profiles nondimensionalized this way. The collapse of the data onto nearly one curve shows the self-similarity of the turbulent boundary layer velocity profiles. The differences between curves is likely due to the inexact estimate for $\delta$ at each location.

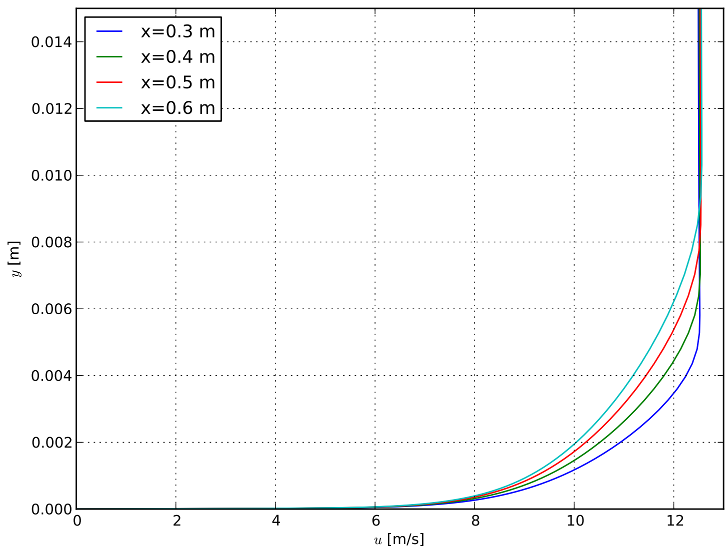


**Figure 4.3.** Single phase velocity profiles at several locations along the plate, $U_\infty = 12.4$ m/s. Continuous growth of the turbulent boundary layer is seen with increasing downstream distance from $x = 0.3$ m (blue) to $x = 0.6$ m (teal) near the downstream end of the force balance.

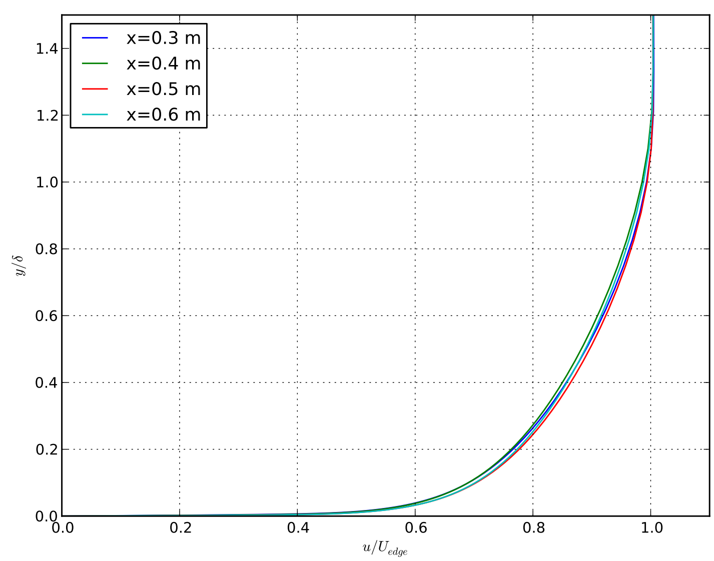


**Figure 4.4.** Single phase velocity profiles in outer variables, $U_\infty = 12.4$ m/s. Collapse of velocity profiles shows the similarity of the TBL velocity distribution when normalized by boundary layer thickness $\delta$.

The velocity profiles from Figure 4.3 are also nondimensionalized by scales characteristic of the innermost region of the TBL, where the influence of the wall is dominant. These scales are formed from the wall shear stress, fluid density and viscosity, and distance from the wall. Figure 4.5 plots a single velocity profile at $x = 0.5$ m in 'inner variables' with a logarithmic $x$-axis. This is done so that the logrithimic region of the mean velocity profile, given by the red curve, will appear as a straight line. This logrithmic region occurs in the overlap between the inner and outer regions, where the effects of the mean flow and the wall balance each other. Values for the logarithmic region, known as the law-of-the-wall, are those suggested by White (1991), $\kappa = 0.41$ and $B = 5.0$. The excellent agreement between the law-of-the-wall and computational results shows that the turbulence model is well calibrated to these conditions.

The green curve shows the relation that dominates in the viscous sublayer, where mean velocity is proportional to distance from the wall. At high $y^+$ values, the mean velocity deviates above the logarithmic curve. This deviation is known as the 'velocity defect', indicating that the influence of the wall is negligible at this distance from the wall.

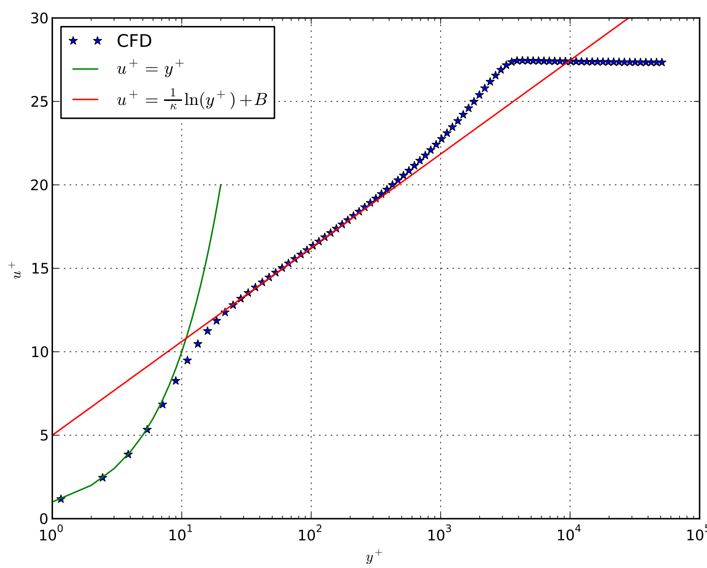


**Figure 4.5.** Single phase velocity profile in inner variables at $x = 0.5$ m, $U_\infty = 12.4$ m/s shows close agreement between: CFD and viscous sublayer relation (green), CFD and the law of the wall (red).

### 4.1.6 Single phase skin friction

The computed shear stress distribution at the wall, $\tau_w$, is shown in Figure 4.6. While discontinuous at the origin, wall shear decreases with increasing $x$ as expected. To validate the predicted wall shear, it is nondimensionalized and compared with two flat plate correlations, as shown in Figure 4.7. The green curve is the correlation suggested by White (1991, pg. 432) which is "recommended as a more or less 'exact' relation for flat-plate turbulent skin friction" and is used as the standard of comparison by Madavan et al. (1984). The red curve is the correlation of Schultz-Grunow, as reported by Elbing et al. (2008). The computational result is seen to lie between the two classical correlations, and is slightly closer to the relation of White. The computational result also flattens out at the end of the domain, most likely due to the zero-gradient boundary condition on velocity, $\partial u/\partial x = 0$, imposed at the outlet.

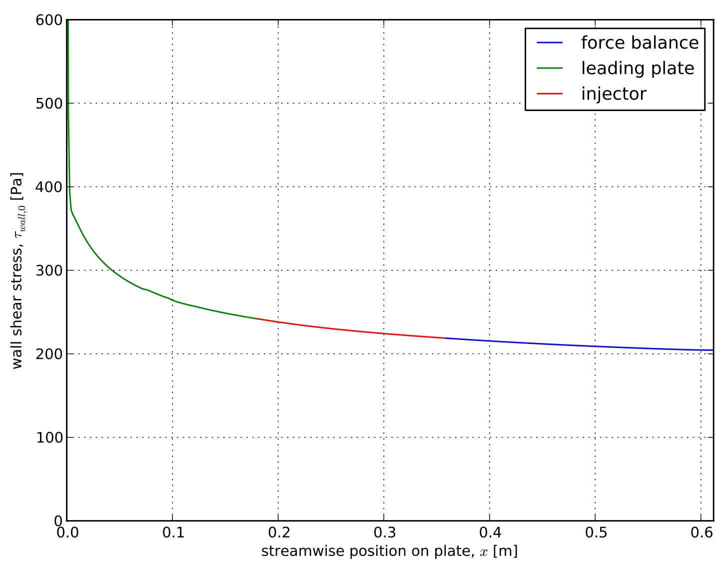


**Figure 4.6.** Single phase wall shear stress profile across the plate, $U_\infty = 12.4$ m/s. Decrease in wall shear with increasing $x$ corresponds to the thickening of the turbulent boundary layer with downstream distance.

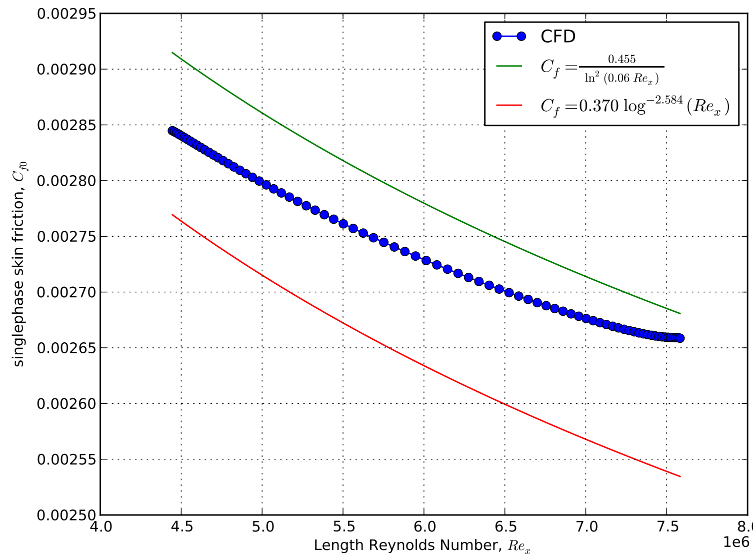


**Figure 4.7.** Single phase computed and empirical skin friction on force balance, $U_\infty = 12.4$ m/s. The CFD curve is bounded by the classical skin-friction relations of White (green) and Schultz-Grunow (red), suggesting the CFD result is within the expected range.

## 4.2 Multiphase simulations

In examining the multiphase simulation results, the primary interest is in how the drag values change when air is injected into the domain. However, we also examine the results to see how the details of the predicted flow compare with the experimental results of the literature review. Of interest are the skin friction, velocity and gas fraction distributions that result from the simulations, and how each of these compare with experimental findings. The effect of plate orientation and strength of the turbulent dispersion are also examined.

### 4.2.1 Case setup and test matrix

The initial condition for each multiphase case is the steady, single phase, flat-plate TBL at the same speed. The singlephase results of the previous section are typical of the initial conditions for multiphase cases. In the simulations gravity is oriented downward toward the injection side, simulating injection below the boundary layer. This is the orientation used to collect the data used here for comparison. Air injection simulations are performed at the four volumetric flow rates given in Table 4.3.

The last column, $v_n$, is the normal velocity corresponding to each flow rate, $v_n = Q/A$, where $A = 0.018156$ m$^2$ is the area of gas injection. At $t = 0$, the volume source of air is activated at the injector of Figure 4.2. To lessen the induced pressure waves and help reach a steady state quickly, the source term is increased in a linear ramp from zero to its full value of $v_n$ over a time of 0.01 s, after which time the value is held constant. The distribution of the source term is spatially uniform across the injector, which assumes the gas flux through the porous plate to be uniform, the simplest possible assumption. The boundary conditions on all the other flow variables, including pressure, velocity and turbulence are the same as in single phase cases.

Twelve multiphase cases were run, by injecting each volumetric gas flow rate from Table 4.3 into turbulent boundary layer flows at each of the three speeds in Table 4.2. The parameter

**Table 4.3.** Air flow rates

| Injection Level | $Q$ [m$^3$/s] | $v_n$ [m/s] |
|---|---|---|
| Q1 | 0.001 | 0.0550782 |
| Q2 | 0.002 | 0.110156 |
| Q3 | 0.003 | 0.165235 |
| Q4 | 0.004 | 0.220313 |

$C_q = Q/AU_\infty$ is given for each of these cases in Table 4.4. This range of $C_q$ values is comparable to that of Kunz et al. (2003) who use six values from 0.0025 to 0.0400, all at the single speed of 10.9 m/s. The gas can be introduced one of two ways:

**Table 4.4.** $C_q$ values for air injection cases

| $U_\infty$ [m/s] | Q1 | Q2 | Q3 | Q4 |
|---|---|---|---|---|
| 9.3 | 0.0059 | 0.0118 | 0.0178 | 0.0237 |
| 12.4 | 0.0044 | 0.0089 | 0.0133 | 0.0178 |
| 17.4 | 0.0032 | 0.0063 | 0.0095 | 0.0127 |

1. *Fixed velocity*: At the injector the gas volume fraction is fixed, $\alpha_1 = 1$, and the boundary velocity is prescribed as $\mathbf{u} = (0\ v_n\ 0)$, where $v_n$ is given in Table 4.3. The source term is set to zero: **source** $= (0\ 0\ 0)$.

2. *Fixed source*: At the injector the gas volume fraction is set to zero-gradient, no-slip velocity is imposed, $\mathbf{u} = (0\ 0\ 0)$, and the source is prescribed: **source** $= (0\ v_n\ 0)$.

All of the multiphase results presented in this thesis use the *fixed source* method (2) above. Comparisons show that there are negligible differences in the computed flow fields and drag values when using the fixed velocity method instead of the fixed source method for air injection. The conditions on all other boundaries are the same in single phase and multiphase simulations. Table 4.5 gives the properties specified for the gas (air) in the multiphase injection simulations.

**Table 4.5.** Air properties specified for multiphase simulations

| symbol | variable | value | units |
|---|---|---|---|
| $\nu_g$ | kinematic viscosity | $1.536 \times 10^{-5}$ | m$^2$/s |
| $\gamma$ | ratio of specific heats | 1.4 | – |
| $a_c$ | adiabatic constant | 101325 | kg $^{-0.4}$ m$^{3.2}$ s $^{-2}$ |

### 4.2.2 Gas concentration profiles

Representative gas fraction profiles, $\alpha(y)$, are shown in Figure 4.8. These two gas fraction profiles are taken downstream of the injector. The profiles do not show the return to zero gas fraction at the wall as seen in the experimental measurements. An explanation for this is that the homogeneous model transports the gas fraction values downstream from the injector; the gas fraction equation is simply a convection-diffusion scalar transport equation, which does not include bubble forces due to the relative velocities between bubbles and the liquid. The high lift forces at the wall from the sharp velocity gradient do not appear in this model.

The effect of the turbulent dispersion term is to mix the phases together. This can be seen in Figure 4.8 as the void fraction near the wall has decreased, while further from the wall it has increased, in moving downstream from 0.4 m to the end of the domain. This movement of air away from the wall can be considered to represent the bubble cloud's movement away from the surface and attendant increase in liquid fraction near the wall. In the context of the current model, the mixture properties near the wall, especially density and viscosity, are slowly returning to those of water as we progress downstream, and therefore lead to the increase of wall shear towards its single phase (no-injection) value.

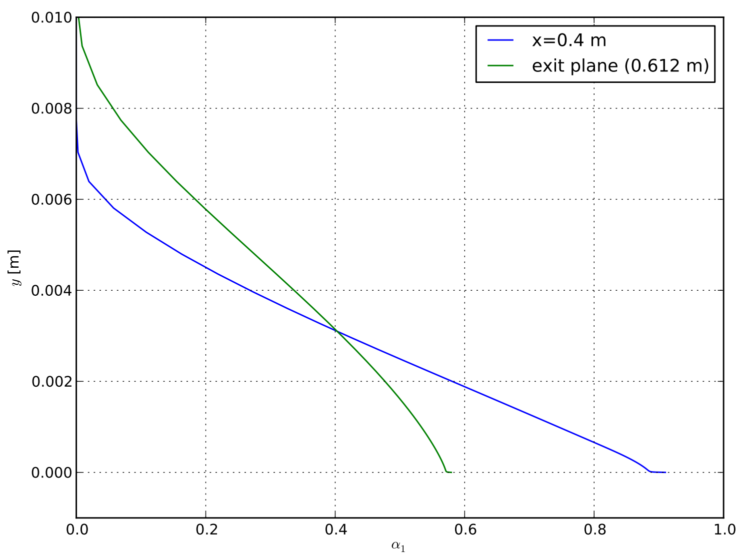


**Figure 4.8.** Gas fraction profiles $\alpha(y)$, $U_\infty = 12.4$ m/s, $Q = 0.003$ m$^3$/s. The gas fraction gradient $d\alpha_1/dy$ is lower at $x = 0.612$ m (green) compared $x = 0.4$ m (blue) because turbulent dispersion has acted to mix the phases.

### 4.2.3 Velocity profiles

Two velocity profiles from the same case and streamwise locations are shown in Figure 4.9. The blue curve shows a velocity profile with a steep velocity gradient to the wall. The green curve shows the mean velocity profile at the exit plane, which looks more typical of a single phase TBL. Increased volume flux near the wall from injection could be responsible for the steeper gradient. Thus, the addition of gas causes substantial modifications to the velocity field near the injector, but the velocity begins to resemble that of a single phase TBL more and more moving downstream from the injection region.

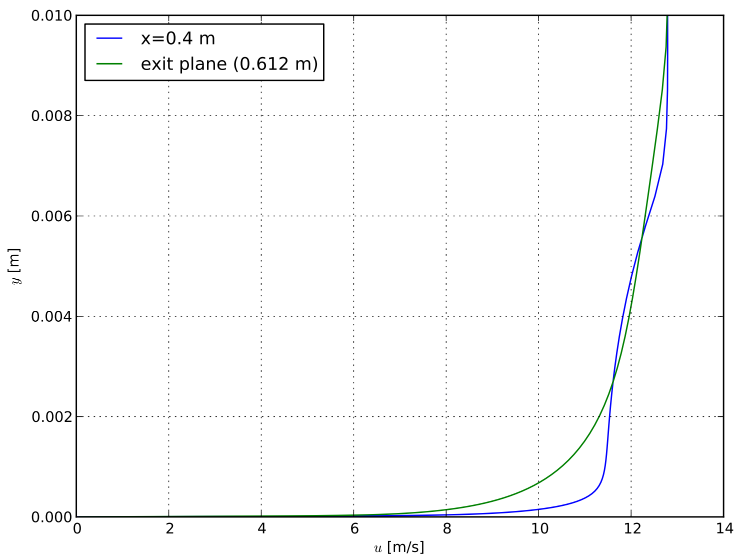


**Figure 4.9.** Velocity profiles $u(y)$, $U_\infty = 12.4$ m/s, $Q = 0.003$ m$^3$/s. The velocity gradient at the wall has decreased significantly between $x = 0.4$ m (blue) and $x = 0.612$ m (green).

### 4.2.4 Wall shear profiles

The distribution of computed wall shear stress for a freestream velocity of $U_\infty = 12.4$ m/s and injection rate of $Q = 0.003$ m$^3$/s is shown in Figure 4.10. Wall shear stress upstream of the injector is relatively unaffected by air injection, while it becomes zero at the injector, and rises gradually with downstream distance along the force balance. The density effect overwhelms all the other flow dynamics in determining the wall shear stress, which is why the shear stress on the injector is nearly zero.

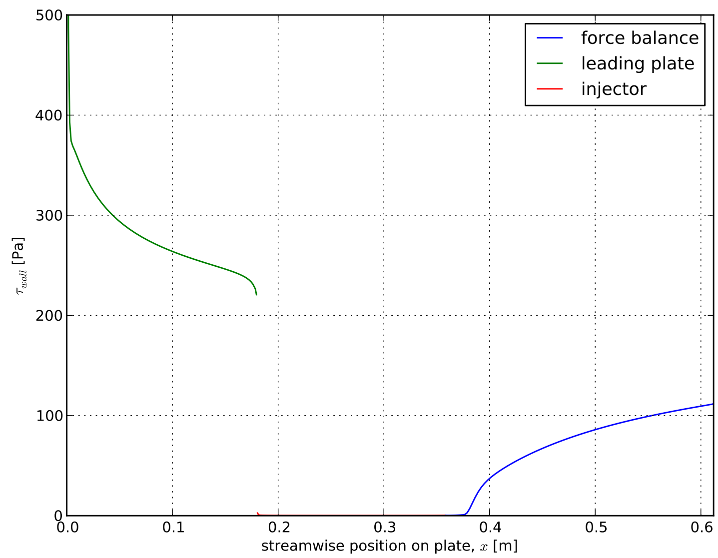


**Figure 4.10.** Wall shear stress along test surface, $U_\infty = 12.4$ m/s, $Q = 0.003$ m$^3$/s. Wall shear is relatively unaffected upstream of injection (green), while it is reduced substantially along the injector and force balance (blue), where it rises monotonically with downstream distance.

### 4.2.5 Dispersion coefficient study

The dispersion coefficient controls the strength of turbulent mixing between phases, and is expected to have a strong effect on the total drag in the simulations. A study was made of one case, at $U_\infty = 12.4$ m/s and $Q = 0.003$ m$^3$/s by varying $C_{\text{disp}}$ in increments of 0.1. It was expected that drag would increase with increasing dispersive action mainly because the mixing would increase the fluid density along the force balance downstream of injection. The result of this study is presented in Figure 4.11. Drag actually decreased as $C_{\text{disp}}$ increased from 0 to 0.1 for an unknown reason. The expected trend emerged as $C_{\text{disp}}$ increased past 0.2. The green line on the figure shows the experimental drag ratio which is 0.45 for this case. This parameter study shows that the dispersion coefficient is tunable, and that a value of $C_{\text{disp}} = 1.3$ would provide a better fit to the data than one, the nominal value for this parameter.

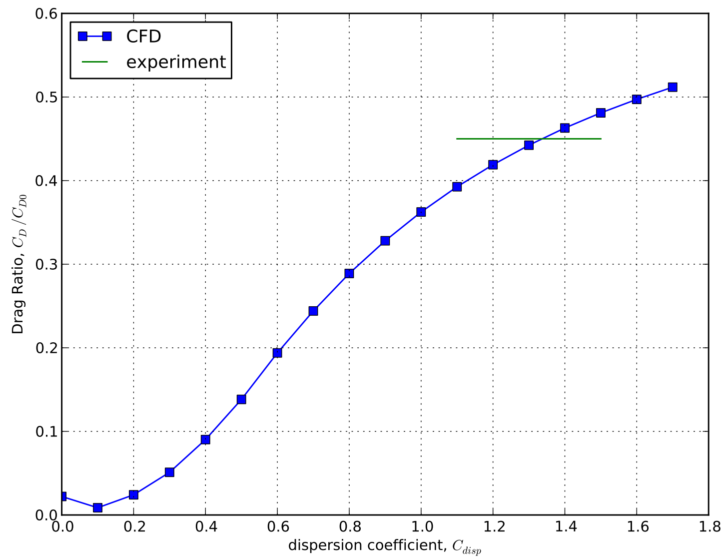


**Figure 4.11.** Drag ratio as a function of $C_{\text{disp}}$, $U_\infty = 12.4$ m/s, $Q = 0.003$ m$^3$/s. Experimental drag ratio (green) corresponds to a simulation with $C_{\text{disp}} \approx 1.3$.

### 4.2.6 Gravitational effects

To study the effect of gravitational orientation of the plate on drag, three cases were run with gravity reversed, simulating the plate below the boundary layer, at $U_\infty = 9.3$, 12.4 and 17.4 m/s, and $Q = 0.003$ m$^3$/s. The three cases were also run with gravity turned off, for an intermediate case. Madavan et al. (1985a) report that plate orientation has a strong effect on drag, with higher drag for the plate on bottom, as illustrated by Figure 2.6. The results shown in Figure 4.12 show no noticeable difference in drag with orientation. This is likely due to the stability of the air-water interface. In the actual flow, individual bubbles are moving through the water, and respond to the buoyant force with a net movement away from the plate when it is located below the boundary layer. The model, however, treats the entire flow as one fluid with no slip between contents and with one velocity field. The presence of the much lighter air beneath the water is an instability which would tend to mix the phases, but the strong convection in these flows is stabilizing, and prevents mixing from the buoyant forces. The inability of the model to respond to changes in gravity is one of its shortcomings.

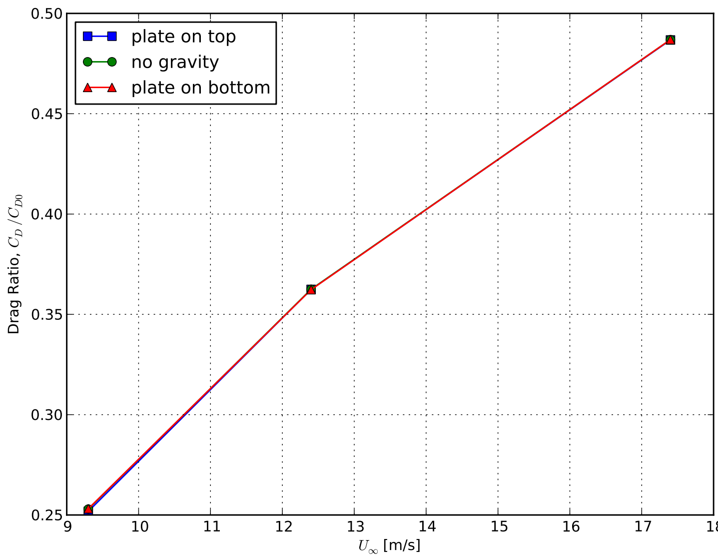


**Figure 4.12.** Drag ratio vs. changing plate orientation, $Q = 0.003$ m$^3$/s. Simulations predict negligible change in drag ratio with change in plate orientation.

### 4.2.7 Drag results

The drag ratio results at $U_\infty = 9.3$, 12.4 and 17.4 m/s and at the four gas injection rates are compiled and compared with experimental results of Madavan et al. (1984) in Figure 4.13. The simulation results making up this figure are oriented with the plate above the boundary layer and $C_{\text{disp}} = 1$. The major trends in drag ratio with injection rate and mean velocity are captured. For a fixed speed, the drag ratio decreases with increasing air injection rate. Also, at a given air injection rate, the drag ratio is lower at lower speeds. This is because more air is present in the boundary layer at higher $C_q$ values, where the air injection rate is more significant compared to the advection of the mean flow. The predicted drag results are in good agreement with experiment, and generally predict a lower drag ratio than seen experimentally.

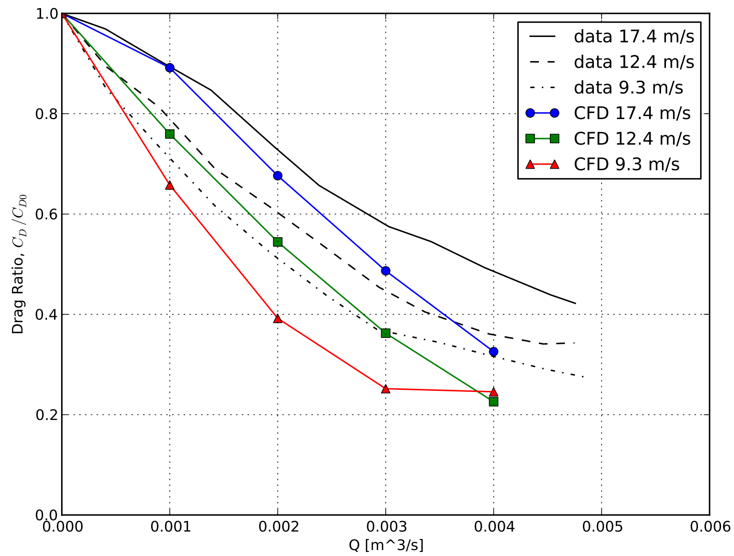


**Figure 4.13.** Comparison of experimental and computed drag ratios at three freestream speeds and four injection rates. Simulations generally predict slightly lower drag ratios than experiments.

The results of Figure 4.13 are presented with the gas injection rate nondimensionalized to $C_q$ values in Figure 4.14. This shows that the same nondimensionalization which is effective in collapsing the experimental results (black) is also effective in collapsing the computational results (blue, green and red). The simulations generally predict lower drag ratios than the experiment at higher $C_q$ values, but generally are in good agreement.

All of the results presented up to this point have been obtained using sublayer-resolved meshes, as explained in the single-phase section. However, from a practical standpoint, it is often desirable to run simulations with much coarser mesh resolution at the wall by using wall functions to account for the near-wall physics of the turbulent boundary layer flow. Since no detailed modeling of the two-phase flow is made here, such as accounting for interfacial forces between bubbles and the liquid, a few test cases were made using wall functions to see how they compare with the sublayer-resolved meshes. Figure 4.15 shows a comparison of the drag ratio using the two meshes at 12.4 m/s and the four injection rates. It is seen that the wall function meshes provide very similar results to the sublayer resolved meshes. The implication is that the density effect and turbulent dispersion effects are captured equally well with the two approaches, and that such wall function meshes are sufficient for practical simulations.

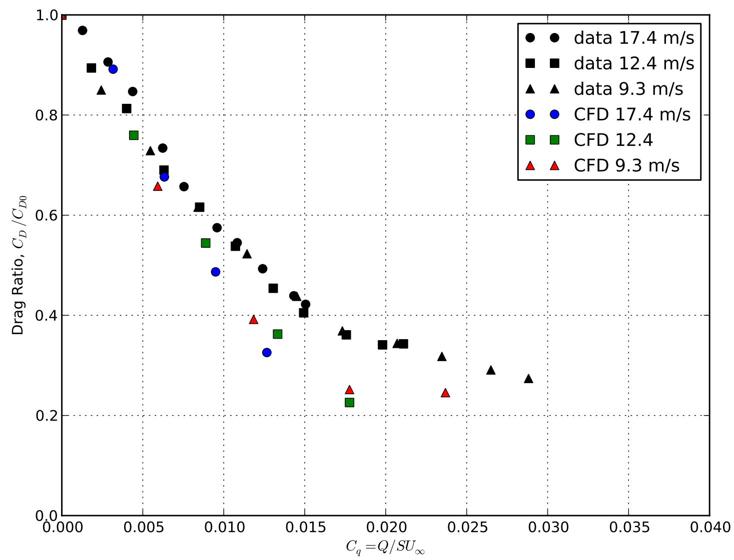


**Figure 4.14.** Experimental and computed drag ratios vs. $C_q$, which is effective in collapsing both experimental and computational drag ratios.

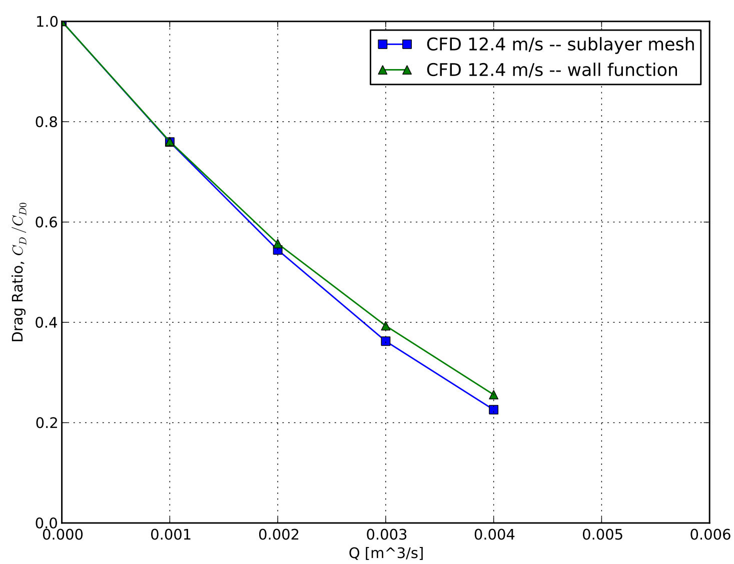


**Figure 4.15.** Comparison of sublayer and wall function mesh drag ratios. Simulations using wall functions (green) produce very similar drag ratios to sublayer-resolved simulations (blue).

Chapter 5

# Summary

An understanding of the physics of microbubble drag reduction is gained through an examination of the literature. Experimental work establishing the drag reduction effect and many of its characteristics is reviewed, along with several proposed mechanisms by which the microbubbles bring about the reduction in drag. This is a very complex problem involving details of microbubble formation, turbulence modification and bubble splitting, all in the context of a compressible, two-phase turbulent boundary layer flow. Despite the complexity of the problem, the reduction of mixture density due to the locally high gas volume fraction near the wall is identified as the dominant mechanism causing the observed reductions in local skin friction. The skin friction increases downstream of the injection region as the near-wall region is depleted of microbubbles by the action of lift forces and turbulent dispersion.

A compressible, homogeneous, two-phase flow solver is applied to the problem of predicting the drag in turbulent boundary layer flows with gas injection from the surface. This formulation captures the reduction in skin friction due to the low mixture density in the near-wall region. The addition of a turbulent dispersion term allows for mixing of the phases in this homogeneous flow model, leading to the gradual decrease of gas volume fraction near the wall and attendant increase in skin friction. The combination of these two effects leads to a successful first-order model for microbubble drag reduction.

However, some of the physics of MBDR flows are not included in this model, namely bubble dynamics. In this homogeneous approach, the microbubble cloud is approximated as a region of high gas fraction, and none of the air-water interfaces (bubbles) are resolved. In the actual flow, the relative velocities between bubbles and the liquid gives rise to lift and drag forces on the bubbles, which along with gravity determine their trajectories from the injection point. This in turn determines the gas fraction near the wall, which is the most important determinant of both the strength and persistence of skin friction reduction. Further, bulk compressibility and bubble splitting, which are theorized to reduce turbulence, are not included in this model. Fortunately, the predominance of the density reduction effect allows this homogeneous model to be successful.

## 5.1 Computational results

The results of Chapter 4 show this model to be in good qualitative and quantitative agreement with the experimental drag reductions recorded by Madavan et al. (1984). The flat plate simulations with gas injection all resulted in similar but somewhat lower drag ratios than experiments. The maximum difference in drag ratio was 16%. Thus, the primary goal of this model, correct prediction of total drag force, has been achieved with reasonable accuracy.

Prediction of lower drag ratios by CFD than experiment indicates that turbulent dispersion alone is not sufficient to bring about the rapid return to singlephase skin friction observed in experiments. Specifically, the lack of lift forces on bubbles is related to the slow decrease in gas fraction near the wall. A parametric variation in $C_{\text{disp}}$ shows that predicted drag can be increased by increasing $C_{\text{disp}}$. However, this amounts to increasing the strength of the dispersion effect to account for another effect absent from model, i.e. lift forces on the bubbles.

The near-wall gas fraction is unity at the injection location, and decreases monotonically downstream. Also, the gas is distributed away from the plate due to the action of turbulent dispersion, leading to a gentle gradient in gas fraction downstream of injection, instead of a sharp air-water interface. This is representative of the bubble cloud dispersing with a net movement away from the wall. The skin friction ratio is nearly zero at the beginning of the force balance section and increases downstream. This trend is consistent with experimental results that skin friction returns to its undisturbed value downstream of injection.

The key trends in skin friction with injection seen experimentally (Madavan et al., 1985a) are also captured by this model. Skin friction decreases with increasing gas injection rates. Also, at higher speeds a higher gas flux is required to obtain the same reduction in skin friction. The skin friction is lowest near the injection region, and increases downstream towards its single phase value.

## 5.2 Future work

With the successful validation of this model against the data of Madavan et al. (1984), it can be applied to six degree-of-freedom simulations of underwater vehicles with gas injection. This will allow for more accurate simulations and resulting trajectories, as an account is now made of the effect of injected gases on surface forces.

Improvements can be made to this homogeneous model. One effect of microbubbles is to increase the mixture molecular viscosity. This can be modeled by incorporating a mixture viscosity formulation from the literature, such as that of Einstein or Sibree. However, neither of these formulations was obtain specifically for MBDR flows. Hence, obtaining a more appropriate mixture viscosity formulation for MBDR flows and incorporating it into this flow model would be appropriate. Turbulence modification ideas (Legner, 1984) can be used to develop a mixing-length turbulence model specifically for these flows. Inclusion of such a turbulence model would make this approach more complete.

Appendix A

# Analysis of Kolmogorov scales with microbubble injection

Motivated by the suggestion that changes in the mixture viscosity lead to a reduction of the smallest scales of turbulence (Lumley, 1973; Madavan et al., 1984), the change in these scales is examined.

The cascade process in turbulent flows is the transfer of turbulent kinetic energy per unit mass, $k$, from larger to successively smaller and smaller eddies. Dissipation of the turbulent energy into heat finally occurs at the smallest scales by the action of the fluid viscosity. The smallest eddies move on a short time scale, and thus are independent of the large-scale motions. Kolmogorov's (1941) universal equilibrium theory assumes that the smallest eddies dissipate energy at the rate it is generated by the largest eddies, $\epsilon = -dk/dt$. Then, the motion at the smallest scales is determined by $\epsilon$ and kinematic viscosity $\nu$. Length ($\eta$), time ($\tau$) and velocity ($v$) scales, called the Kolmogorov microscales of turbulence, emerge by combining $\epsilon$ and $\nu$ (Wilcox, 1998).

$$\eta = (\nu^3/\epsilon)^{1/4} \tag{A.1a}$$

$$\tau = (\nu/\epsilon)^{1/2} \tag{A.1b}$$

$$v = (\nu\epsilon)^{1/4} \tag{A.1c}$$

Using the 0 subscript for the singlephase flow and $m$ for the mixture flow with microbubbles, we take the ratio of the modified scales to the unmodified scales. If we assume that the large-scale structure of the turbulence is unaffected by the microbubbles, then $\epsilon_m = \epsilon_0$. This assumption is supported by the conclusions of Madavan et al. (1984):

> Velocity and turbulence intensity profiles in the outer region of the boundary layer show no dramatically different character when microbubbles are present as compared to when they are absent. This lends credence to the concept of a boundary layer modified by the presence of microbubbles as opposed to a complete restructuring of

the flow field when the microbubbles are introduced.

The generation of turbulence energy occurs by generation of the largest eddies, far from the wall by the mean velocity gradient, e.g. exactly where Madavan et al. (1984) tell us that the flow is not altered by the presence of bubbles. Now, the ratio between the scales only depends on the kinematic viscosity ratio:

$$\frac{\eta_m}{\eta_0} = \left(\frac{\nu_m}{\nu_0}\right)^{3/4} \tag{A.2a}$$

$$\frac{\tau_m}{\tau_0} = \left(\frac{\nu_m}{\nu_0}\right)^{1/2} \tag{A.2b}$$

$$\frac{\upsilon_m}{\upsilon_0} = \left(\frac{\nu_m}{\nu_0}\right)^{1/4} \tag{A.2c}$$

The mixture kinematic viscosity depends on the molecular viscosity and density by definition,

$$\nu_m = \frac{\mu_m}{\rho_m}. \tag{A.3}$$

With $\rho_{air} \ll \rho_0$, the mixture density becomes

$$\rho_m \approx (1-\alpha)\rho_0. \tag{A.4}$$

Since molecular viscosity of air is much less than that of water, the effect of air bubbles is to increase the mixture viscosity independently of the air viscosity, as seen in (2.14) and (2.9). Then, mixture to singlephase molecular viscosity ratio can similarly be expressed as a function of gas fraction alone, and

$$\frac{\nu_m}{\nu_0} = \xi(\alpha) \tag{A.5}$$

is the controlling parameter for the microscales, whose ratios can be rewritten as

$$\frac{\eta_m}{\eta_0} = [\xi(\alpha)]^{3/4} \tag{A.6a}$$

$$\frac{\tau_m}{\tau_0} = [\xi(\alpha)]^{1/2} \tag{A.6b}$$

$$\frac{\upsilon_m}{\upsilon_0} = [\xi(\alpha)]^{1/4} \tag{A.6c}$$

Choosing Einstein's viscosity relation, (2.14), the kinematic viscosity ratio becomes

$$\xi_1(\alpha) = \frac{1+2.5\alpha}{1-\alpha}. \tag{A.7}$$

If Sibree's relation (2.9) is used, then we have

$$\xi_2(\alpha) = \frac{1}{(1-1.09\alpha^{1/3})(1-\alpha)}. \tag{A.8}$$

The effect of the gas fraction on the microscales is plotted in Figure A.1. This shows clearly that all the microscales of turbulence become larger as a result of the changing mixture properties. What this really means is that the higher mixture viscosity is able to smear out increasingly larger eddies, and so the total turbulent kinetic energy, $k$, is reduced locally. For example, at a gas fraction of 50%, this analysis predicts the size of the smallest eddies will be between three and eight times larger than in the corresponding flow without microbubbles, assuming the actual solution viscosity to be bounded by the two relations used here.

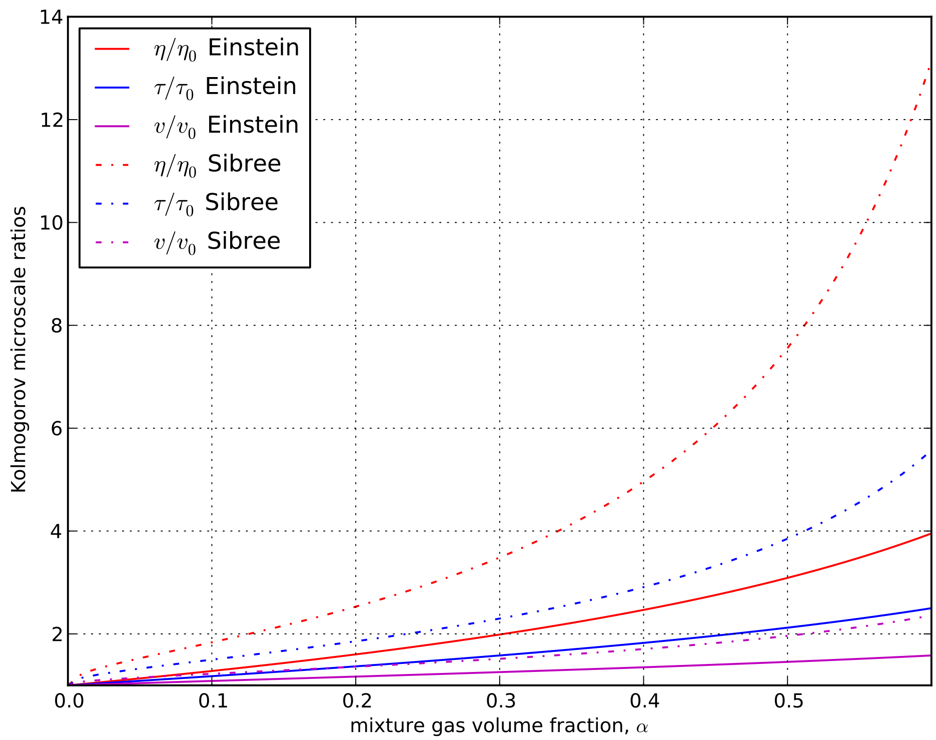


**Figure A.1.** Change in microscales of turbulence with increasing gas volume.

These results confirm the theoretical conjectures of Lumley (1973) and observations of Madavan et al. (1985a), whose hot-film signals showed a loss of high frequency content. This loss of small scale turbulence is reflected in a reduced turbulence Reynolds number,

$$Re_T = \frac{k^{1/2} l}{\nu}, \tag{A.9}$$

where $l$ is the size of the largest eddies in the flow, of the same order of size as the boundary layer thickness $\delta$.

The disappearance of the smallest scales of turbulence is a recurring theme in the literature. Two mechanisms leading to this have been presented: increased mixture viscosity, as demonstrated here, and the bubble splitting mechanism of Meng & Uhlman (1998). It is likely that both mechanisms are active in turbulent boundary layers with microbubble injection, so determining which is stronger may be difficult. In any case, this destruction of turbulence seems to be the key to the drag reduction, regardless of physical mechanism.

# Bibliography


Boger, D. (2004). Notes for setting grid wall spacing. personal communication.

Elbing, B., Winkel, E., Lay, K., Ceccio, S., Dowling, D., & Perlin, M. (2008). Bubble-induced skin-friction drag reduction and the abrupt transition to air-layer drag reduction. *Journal of Fluid Mechanics*, **612**(1), 201–236.

Ferziger, J. & Perić, M. (2002). *Computational Methods for Fluid Dynamics, 3rd Ed.* Springer-Verlag.

Fontaine, A. & Deutsch, S. (1992). The influence of the type of gas on the reduction of skin friction drag by microbubble injection. *Experiments in fluids*, **13**(2), 128–136.

Incropera, F., DeWitt, D., Bergman, T., & Lavine, A. (2007). *Fundamentals of Heat and Mass Transfer, 6th edition*. Wiley.

Kunz, R., Deutsch, S., & Lindau, J. (2003). Two fluid modeling of microbubble turbulent drag reduction. In *Proceedings of ASME FEDSM'03*. ASME.

Kunz, R., Gibeling, H., Maxey, M., Tryggvason, G., A.A., F., Petri, H., & Ceccio, S. (2007). Validation of two-fluid eulerian cfd modeling for microbubble drag reduction across a wide range of reynolds numbers. *Journal of Fluids Engineering*, **129**, 66–79.

Legner, H. (1984). A simple model for gas bubble drag reduction. *Physics of Fluids*, **27**, 2788–2790.

Lumley, J. (1973). Drag reduction in turbulent flow by polymer additives. *Journal of Polymer Science: Macromolecular Reviews*, **7**(1), 263–290.

Madavan, N., Deutsch, S., & Merkle, C. (1984). Reduction of turbulent skin friction by microbubbles. *Physics of Fluids*, **27**, 356–363.

Madavan, N., Deutsch, S., & Merkle, C. (1985a). Measurements of local skin friction in a microbubble-modified turbulent boundary layer. *Journal of Fluid Mechanics*, **156**, 237–256.

Madavan, N., Merkle, C., & Deutsch, S. (1985b). Numerical investigations into the mechanisms of microbubble drag reduction. *Journal of Fluids Engineering*, **107**, 370–377.

Marie, J. (1987). A simple analytical formulation for microbubble drag reduction. *PhysicoChemical Hydrodynamics*, **8**(2), 213–220.

Meng, J. & Uhlman, J. (1998). Microbubble formation and splitting in a turbulent boundary layer for turbulence reduction. In *Proceedings of the international symposium on seawater drag reduction*, volume 22, pages 341–355.

Merkle, C. & Deutsch, S. (1992). Microbubble drag reduction in liquid turbulent boundary layers. *Applied Mechanics Reviews*, **45**, 103–127.

Miller, S., Jasak, H., Boger, D., Paterson, E., & Nedungadi, A. (2012). A pressure-based, compressible, two-phase flow fvm for underwater explosions. *Submitted*.

OpenFOAM (2012). Openfoam: The open source cfd toolbox. `http://www.openfoam.com`.

Sanders, W., Winkel, E., Dowling, D., Perlin, M., & Ceccio, S. (2006). Bubble friction drag reduction in a high-reynolds-number flat-plate turbulent boundary layer. *Journal of Fluid Mechanics*, **552**, 353–380.

Sibree, J. (1934). The viscosity of froth. *Transactions of the Faraday Society*, **30**(0), 325–331.

Skudarnov, P. & Lin, C. (2006). Drag reduction by gas injection into turbulent boundary layer: Density ratio effect. *International journal of heat and fluid flow*, **27**(3), 436–444.

Spalart, P. & Allmaras, S. (1994). A one-equation turbulence model for aerodynamic flows. *La recherche aérospatiale*, **1**(1), 5–21.

White, F. M. (1991). *Viscous Fluid Flow, 2nd Ed.* McGraw-Hill.

Wilcox, D. C. (1998). *Turbulence Modeling for CFD, 2nd Ed.* DCW Industries.